8-2010

Along-Strike Growth of the Ostler Fault, New Zealand: Consequences for Drainage Deflection above Active Thrust

Colin B. Amos
Western Washington University, colin.amos@wwu.edu

Douglas W. Burbank

Stuart A. L. Read

Along-strike growth of the Ostler fault, New Zealand: Consequences for drainage deflection above active thrusts

Colin B. Amos,[1,2] Douglas W. Burbank,[1,3] and Stuart A. L. Read[4]

Received 14 September 2009; revised 2 March 2010; accepted 9 March 2010; published 6 August 2010.

[1] Rarely are geologic records available to constrain the spatial and temporal evolution of thrust-fault growth as slip accumulates during repeated earthquake events. Here, we utilize multiple generations of dated and deformed fluvial terraces to explore two key aspects of the along-strike kinematic development of the Ostler fault zone in southern New Zealand over the past ~100 k.y.: accumulation of fault slip through space and time and fixed-length thrust growth that results in patterns of drainage diversion suggestive of laterally propagating faults. Along the Ostler fault, surface deformation patterns revealed by topographic surveying of terrace profiles in nine transverse drainages define systematic variations in fault geometry and suggest deformation over both listric and planar thrust ramps. Kinematic modeling of folded terrace profiles and >100 fault-scarp surveys along major fault sections reveals remarkably similar slip distributions for multiple successions of geomorphic surfaces spanning ~100 k.y. Spatially abrupt and temporally sustained displacement gradients across zones of fault section overlap suggest that either persistent barriers to fault propagation or interference between overlapping faults dominate the interactions of fault tips from the scale of individual scarps to the entire fault zone. Deformed terrace surfaces dated using optically stimulated luminescence and cosmogenic radionuclides indicate steady, maximum rates of fault slip of ~1.9 mm/yr during the Late Quaternary. Slip data synthesized along the central Ostler fault zone imply that displacement accumulated at approximately constant fault lengths over the past ~100 k.y. A northward temporal progression of abandoned wind gaps along this section thus reflects lateral tilting in response to amplification of displacement, rather than simple fault lengthening or lateral propagation. Oscillations of climate at ~10^4-yr time scales modulate the formation and incision of geomorphic surfaces during successive glacial stages. Superimposed on apparently steadier rates of fault slip, such climate-dependent surfaces contribute to a pattern of progressive drainage deflection along the central Ostler fault zone that is largely independent of fault propagation. **Citation:** Amos, C. B., D. W. Burbank, and S. A. L. Read (2010), Along-strike growth of the Ostler fault, New Zealand: Consequences for drainage deflection above active thrusts, *Tectonics*, *29*, TC4021, doi:10.1029/2009TC002613.

1. Introduction

[2] A quantitative understanding of thrust fault growth remains integral to our knowledge of how active compressional mountain belts evolve during ongoing deformation and crustal shortening. Actual kinematic constraints on the three-dimensional, spatiotemporal development of active thrust systems, however, are surprisingly scarce. Both geomorphic surfaces and syntectonic sediments have emerged as useful archives of strain by linking the kinematic predictions of thrust fault-related folding (i.e., fault-bend, fault-propagation, and trishear models) [*Suppe*, 1983; *Suppe and Medwedeff*, 1990; *Erslev*, 1991] to active deformation of the ground surface [e.g., *Lavé and Avouac*, 2000; *Thompson et al.*, 2002; *Hardy and Poblet*, 2005; *Dolan and Avouac*, 2007, and references therein]. Despite their role in providing constraints on the style, rate, and magnitude of active thrusting from topographic and seismic data, such studies typically present a two-dimensional, transport-parallel view into the growth and architecture of active thrust systems. The tendency for thrusts to lengthen with increasing displacement [e.g., *Elliott*, 1976; *Walsh and Watterson*, 1988; *Cowie and Scholz*, 1992], however, underscores the necessity of both transport-parallel and -perpendicular perspectives in providing a comprehensive view of thrust fault evolution [*Cooper et al.*, 2003; *Bernal et al.*, 2004].

[3] By exploiting linkages between thrust faulting and folding of the Earth's crust [e.g., *Boyer and Elliot*, 1982], numerous studies have utilized along-strike analysis of active fault-related folds as a proxy for delineating thrust growth in three dimensions [e.g., *Jackson et al.*, 1996; *Mueller and Talling*, 1997; *Delcaillau et al.*, 1998; *Bull*, 2009]. Such studies typically rely on combined structural and geomorphic analyses of emergent folds and chronologic constraints on deformed geomorphic surfaces [*Keller et al.*, 1998; *Jackson et al.*, 2002; *Hetzel et al.*, 2004; *Bennett et al.*, 2005, 2006], magnetostratigraphy of growth strata

[1]Department of Earth Science, University of California, Santa Barbara, California, USA.
[2]Now at the Department of Earth and Planetary Science, University of California, Berkeley, California, USA.
[3]Institute for Crustal Studies, University of California, Santa Barbara, California, USA.
[4]Institute of Geological and Nuclear Sciences Ltd., Lower Hutt, New Zealand.

0278-7407/10/2009TC002613

[*Chen et al.*, 2002, 2007], or ergodic, space-for-time substitutions [*Burbank et al.*, 1999; *Keller et al.*, 1999] to document growth histories along the underlying active thrusts. Taken together, these studies suggest that thrust fault growth is often nonlinear, and that rates of lateral thrust propagation can be rapid (10 s of mm/yr) and variable with respect to the total fault displacement [*Bennett et al.*, 2006]. Such data fill a crucial gap in our understanding of the evolution of fault length and displacement relationships, given that kinematic constraints on competing models for fault growth are generally absent [*Walsh et al.*, 2002]. Slip histories constructed from both active and inactive fault systems, however, are generally ambiguous as to whether they reflect lateral fault growth or sustained displacement gradients on the controlling thrust [*Keller et al.*, 1999]. The actual kinematics of displacement transfer and segment linkage for active thrusts are also confounded by insufficient temporal control [*Davis et al.*, 2005], again highlighting the need for quantitative measures of along-strike thrust fault growth.

[4] Here, we define and analyze patterns of thrust development for the Ostler fault zone, a well-expressed Quaternary thrust fault in southern New Zealand (Figure 1). By integrating kinematic analysis of displaced geomorphic surfaces from nine transverse drainages along the ~60-km surface trace, we delineate spatial patterns of deformation parallel and perpendicular to the fault transport direction. As tools, we combine the results of detailed geomorphic mapping with high-resolution topographic surveying of both deformed geomorphic surfaces and active fault scarps, and with geochronologic constraints on terrace formation. Our synthesis indicates that, over the past ~70–100 k.y., growth of the Ostler fault zone occurred through gradual amplification of the displacement profile without resolvable fault lengthening. Displacement and slip-rate estimates for multiple generations of deformed surfaces along each fault section reveal a range of profile shapes, with either asymmetric or centrally localized maxima and smoothly varying gradients generally steepening toward the fault tips. Steeper and persistent displacement-rate gradients occur at segment boundaries where overlapping fault strands suggest significant slip transfer or incipient linkage.

[5] Maintenance of these displacement-rate gradients through time also contributes to the general northward pattern of drainage deflection and the younging of paleo-outwash valleys preserved along the Ostler fault zone [*Amos and Burbank*, 2007]. In contrast to conventional interpretations of progressive wind-gap emplacement as reflecting lateral fault propagation [*Jackson et al.*, 1996; *Delcaillau et al.*, 1998; *Keller et al.*, 1998; *Burbank et al.*, 1999; *Keller et al.*, 1999], drainage diversion along the Ostler fault instead reflects lateral tilting in response to amplification of the displacement profile in the absence of significant fault lengthening. This result highlights potential discrepancies between rates of drainage diversion and lengthwise fault growth and emphasizes the importance of geochronologic control on the creation of wind gaps in efforts to reconstruct the growth history of active thrusts and related folds.

2. Study Area

2.1. Regional Setting and Background

[6] The Ostler fault represents a zone of east-directed thrusting within the intermontane Mackenzie Basin in the Southern Alps of New Zealand (Figure 1). The fault constitutes one of several structures east of the plate-bounding Alpine fault that accommodate approximately one-quarter to one-third of the ~37 mm/yr of relative motion between the obliquely colliding Pacific and Australian plates [*DeMets et al.*, 1994; *Pearson et al.*, 1995; *Tippett and Hovius*, 2000; *Norris and Cooper*, 2001]. Resolved onto the Alpine fault, this motion corresponds to velocities parallel and perpendicular to the plate boundary of ~35 and ~10 mm/yr, respectively [*Norris and Cooper*, 2001]. The roughly north–northeast-striking Ostler fault is oriented oblique to the direction of plate convergence (Figure 1) in a structural transition zone that interrupts the predominately plate-boundary-parallel orientation of folds and thrusts in the central South Island [*Upton et al.*, 2009]. This zone consists of several north- to northwest-striking reverse faults and isolated sinistral strike-slip faults localized along an inherited, pre-collisional transition in crustal thickness and rheological properties between Otago to the southwest and Canterbury to the northeast [*Upton et al.*, 2009].

[7] The crustal composition and structure of the Mackenzie Basin primarily reflects the assemblage and subsequent tectonic and erosional modification of the Permo-Triassic Torlesse terrane. Ranges surrounding the Mackenzie Basin comprise deformed Torlesse greywacke, foliated metagreywacke, and its low-grade schist equivalent [*Sporli and Lillie*, 1974]. The Torlesse terrane originated within an accretionary prism bounding the convergent margin of Gondwana [*MacKinnon*, 1983]. Later rifting of this margin in the Cretaceous resulted in pervasive extensional deformation of Torlesse rocks and is recorded in a series of Tertiary basins localized along the crustal boundary separating Otago and Canterbury [*Deckart et al.*, 2002; *Upton et al.*, 2009]. Within the Mackenzie Basin, Cretaceous-Miocene sedimentary rocks are nowhere exposed but are interpreted from seismic imaging to rest unconformably above Torlesse basement [*Long et al.*, 2003]. Based on the inferred presence of these deposits at depth, *Ghisetti et al.* [2007] suggest that the Mackenzie Basin may represent an inverted Tertiary extensional basin, controlled by the Ostler fault zone as reactivated normal fault.

[8] Upper portions of the Mackenzie Basin stratigraphy consist of Plio-Pleistocene molasse of the Kurow Group [*Mildenhall*, 2001], recording earlier periods of uplift and unroofing of the Southern Alps [*Chamberlain et al.*, 1999]. Kurow Group sediments are primarily exposed in uplifted and backtilted dip panels above active thrusts in the Mackenzie Basin [*Gair*, 1967]. The modern geomorphic surface of the Mackenzie Basin is dominated by Pleistocene outwash and fluvial gravels, and estimates of basin depth limit the total thickness of Cenozoic deposits to less than 2 km [*Long et al.*, 2003].

[9] The active surface trace of the Ostler fault zone spans ~60 km, from the Ahuriri River in the south (Figure 1) to

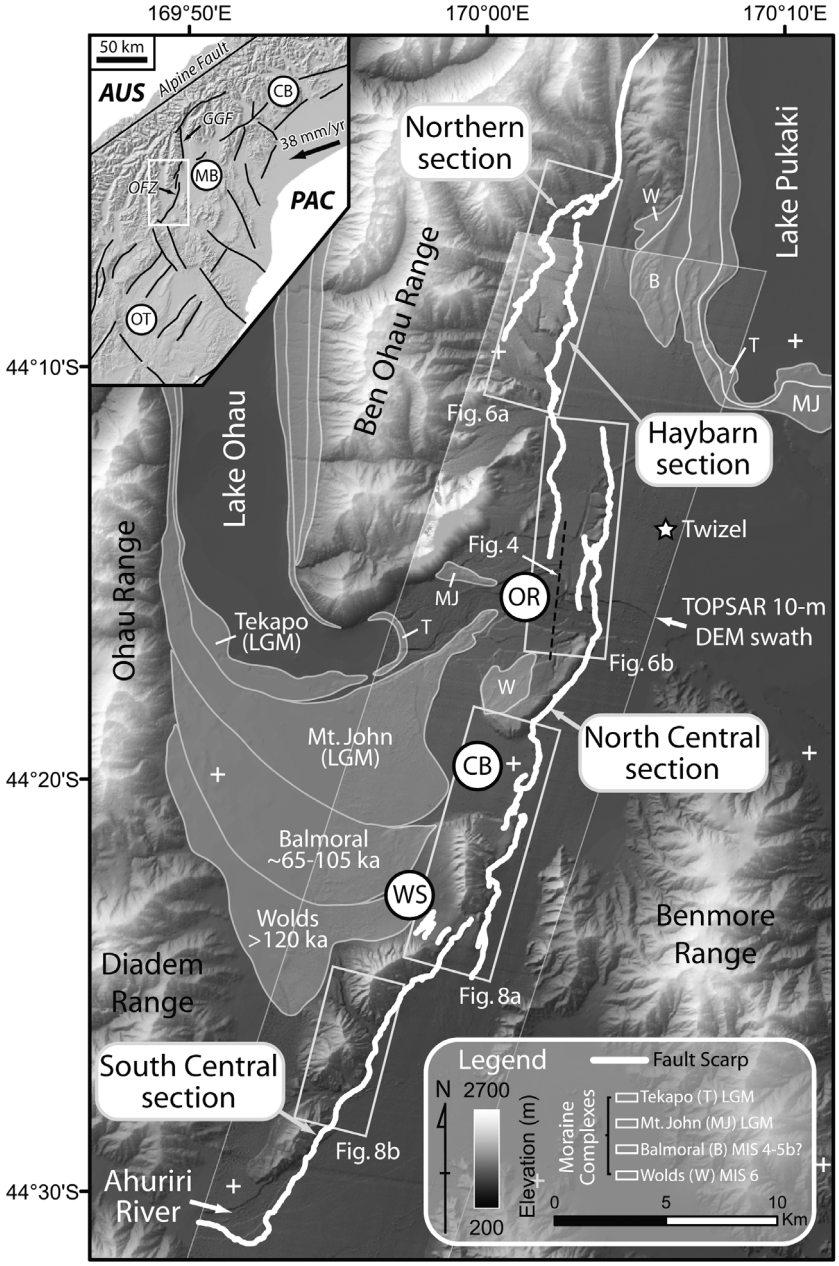

Figure 1. The Ostler fault zone, South Island, New Zealand. Overview map shows the location of fault scarps, major fault section boundaries, and moraine complexes in the Ohau and Pukaki Valleys. Paleo-outwash valleys at Willowbank Saddle (WS) and Clearburn (CB) record progressive northward drainage deflection toward the modern position of the Ohau River (OR). Inset depicts active fault traces in the Mackenzie Basin (MB), Otago (OT), and Canterbury (CB), as well as the tectonic setting of the obliquely colliding Australian (AUS) and Pacific (PAC) plates. The location of the Ostler fault zone (OFZ) within the small bounding box and the Great Groove fault (GGF) are also shown for reference.

Whale Stream at the northern end of Lake Pukaki. To the north, the Ostler fault merges with the Great Groove fault, which extends an additional ~30 km northward along the foot of the Ben Ohau Range [*Ward and Sporli*, 1979]. Complex and highly segmented surface ruptures define four main fault sections along the Ostler fault zone (Figure 1). From north to south, the Northern, Haybarn, North Central, and South Central sections define an average fault strike of 015°. Despite the fault zone's relatively discontinuous surface trace and the presence of several km-scale step-overs (Figure 1), individual sections along the Ostler fault are interpreted as kinematically linked at depth [*Davis et al.*,

2005]. Offset geomorphic surfaces preserved across the fault show primarily west-side-up displacements without a significant component of oblique slip [*Read*, 1984; *Davis et al.*, 2005]. Along the Great Groove fault, however, displacement of Kurow Group sediments includes both reverse and left-lateral strike slip motion [*Templeton et al.*, 1999].

[10] Fault planes imaged using ground-penetrating radar the along the North Central section immediately west of Twizel (Figure 1) have average dips of 56 ± 9° (2σ) in the shallow subsurface [*Amos et al.*, 2007]. These dips generally agree with estimates from offsets of multiple terrace levels (50 ± 18° (2σ)) [*Davis et al.*, 2005] and deeper seismic reflection and refraction data (~50–60°) [*Ghisetti et al.*, 2007; *Campbell et al.*, 2010]. Ground-penetrating radar studies farther south along the North Central section reveal a range in fault dips between ~30° [*McClymont et al.*, 2008] and ~50° [*Wallace et al.*, 2010], indicating some degree of dip variability in the shallow subsurface. Folded geomorphic surfaces in the hanging wall of the Ostler fault zone commonly define highly asymmetric anticlines with broad, west-tilted backlimbs and half-wavelengths of up to several km [*Davis et al.*, 2005]. In an earlier study [*Amos et al.*, 2007], we interpreted this pattern of surface deformation as representing slip along listric, or curviplanar thrusts rooted at shallow depths into planar fault ramps, potentially controlled by the mechanical stratigraphy and depth of Cenozoic basin fill.

[11] Estimates of the total offset on the Ostler fault stem from seismic imaging along the North Central fault section [*Ghisetti et al.*, 2007; *Campbell et al.*, 2010]. Several Plio-Pleistocene sedimentary sequences that are identified and correlated across the fault by *Ghisetti et al.* [2007] yield a total fault throw of ~800 m and a corresponding shortening of ~30%. Constraints on the timing of fault onset are less clear, although *Davis et al.* [2005] suggest a mid-Pleistocene origin for the Ostler fault based on extrapolation of fault length-displacement scaling relationships. Exposed growth strata in the Ostler fault hanging wall (see discussion below and also *Amos et al.* [2007] and *Ghisetti et al.* [2007]) also demonstrate that deformation was clearly ongoing during deposition of Plio-Pleistocene molasse.

[12] Previous work on deformed terraces crossing the Ostler fault zone suggests slip rates in excess of ~1 mm/yr [*Blick et al.*, 1989; *Read and Blick*, 1991; *Davis et al.*, 2005; *Amos et al.*, 2007]. This rate corresponds to ~10% of the distributed Pacific plate motion southeast of the Alpine fault. Geodetically observed vertical deformation of the Ostler fault hanging wall occurs at a similar rate, suggestive of either interseismic storage of elastic strain or aseismic folding [*Blick et al.*, 1989]. Paleoseismic trenching on the northern Ostler fault [*van Dissen et al.*, 1994], however, implies that large, surface-rupturing earthquakes occur along the Ostler fault zone. The timing of these paleoearthquakes between ~3–4 ka, ~6–8 ka, and ~10 ka indicates a recurrence interval of ~2–5 ky for the northern Ostler fault [*van Dissen et al.*, 1994]. Away from transverse drainages, a ~1 m-high scarp cuts the foot of young hillslopes and recent landslide deposits along much of the fault's length and may represent a single-event scarp formed during the most recent earthquake.

2.2. Geomorphology of the Ostler Fault Zone

[13] Several generations of Late Pleistocene glacial moraines, outwash surfaces, and fluvial terraces dominate the surficial geology of the Mackenzie Basin [*Read*, 1984]. Terrace and outwash surfaces are graded to moraine complexes reflecting intermittent glacial occupation of the Lake Ohau and Lake Pukaki valleys [*Blick et al.*, 1989; *Read and Blick*, 1991]. Quaternary landforms and deposits in the Mackenzie Basin were originally categorized through relative dating and field relationships into four major age divisions [*Gair*, 1967]. We build upon this classification scheme and subdivide geomorphic surfaces into Wolds, Balmoral, Mount John, and Tekapo age associations (T1 to T4), from oldest to youngest (Figure 2). Each age association contains multiple terrace levels, noted using apostrophes, e.g., T1′. Dating of terrace surfaces spanning the length of the Ostler fault (discussed below) confirms synchronous times of terrace formation between individual drainages.

[14] Flights of terraces preserved across the Ostler fault represent strath terraces eroded into bedrock, aggradational Quaternary outwash surfaces, or isolated cut terraces beveled into Pleistocene outwash. Exposures into strath terrace surfaces reveal up to several meters of fluvial sand and gravel resting above the bedrock strath. In contrast, terrace surfaces with thicker gravel cover (i.e., ≥~3 m) are classified here as outwash terraces, which are aggradational features. Basal exposures of outwash surfaces are uncommon, although where visible, they indicate on the order of several decimeters or less of overlying gravel cover. Intricate texturing of strath and outwash terrace surfaces with abundant paleochannels attests to their relatively pristine and uneroded nature, despite a locally irregular loess and soil cover typically less than a meter thick [*Maizels*, 1989].

[15] Geomorphic surfaces on the Ostler fault also include three broad, originally flat-bottomed outwash valleys eroded through Plio-Pleistocene bedrock across the North Central section [*Amos and Burbank*, 2007] (Figure 1). The southern two outwash valleys (Willowbank and Clearburn) no longer contain major, active drainages and are preserved as wind gaps uplifted above the basin floor. Westward tilting due to folding over the Ostler fault has locally reversed the original eastward slope of the outwash surfaces in each wind gap. Drainage from the Lake Ohau valley now follows the northernmost valley and crosses the North Central section of the Ostler fault zone immediately south of the town of Twizel (Figure 1).

[16] If we assume that deformed strath terraces formed with a long profile geometry similar to modern streams [*Pazzaglia and Brandon*, 2001], widespread and laterally continuous terrace surfaces preserved across the Ostler fault zone represent ideal, dateable strain markers for recording fault growth. This assumption is most likely to be valid where longitudinal profiles along a strath surface can be compared to the modern bedrock channel, because straths represent former equilibrium positions of the river bed prior to incision [*Bull*, 1991]. For outwash or fill terraces, potential dissimilarities between the initial surface geometry and modern stream profiles are more likely, given that bedrock geometry beneath outwash surfaces is commonly

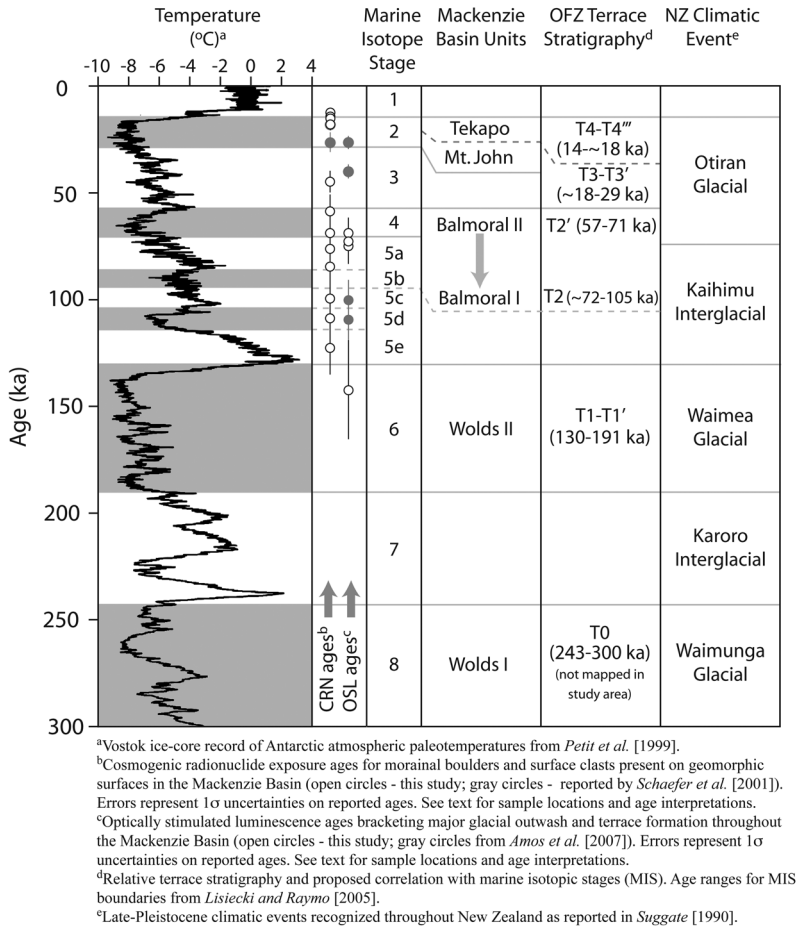

[a]Vostok ice-core record of Antarctic atmospheric paleotemperatures from *Petit et al.* [1999].
[b]Cosmogenic radionuclide exposure ages for morainal boulders and surface clasts present on geomorphic surfaces in the Mackenzie Basin (open circles - this study; gray circles - reported by *Schaefer et al.* [2001]). Errors represent 1σ uncertainties on reported ages. See text for sample locations and age interpretations.
[c]Optically stimulated luminescence ages bracketing major glacial outwash and terrace formation throughout the Mackenzie Basin (open circles - this study; gray circles from *Amos et al.* [2007]). Errors represent 1σ uncertainties on reported ages. See text for sample locations and age interpretations.
[d]Relative terrace stratigraphy and proposed correlation with marine isotopic stages (MIS). Age ranges for MIS boundaries from *Lisiecki and Raymo* [2005].
[e]Late-Pleistocene climatic events recognized throughout New Zealand as reported in *Suggate* [1990].

Figure 2. Terrace stratigraphy/Quaternary chronology for surfaces preserved along the Ostler fault zone. OSL dating of terrace fills from this study and *Amos et al.* [2007] bracket correlation of the Balmoral surface with cold periods during either Marine Isotope Stage 4 or 5b. Mean cosmogenic exposure ages on a Tekapo moraine match well with latest-LGM moraines dated by *Schaefer et al.* [2001, 2006].

unknown, the thickness of outwash gravels may approach tens of meters, and increased sediment load during outwash events probably required a steeper transport gradient. This discrepancy is exemplified by the modern Ohau River, where average long profile slopes on the Mount John outwash surface (~0.9°) exceed modern local river gradients (~0.4°) upstream of the area affected by folding. As such, the actual magnitude of post-abandonment westward (upstream) tilting of this surface is probably underestimated through comparison with the modern channel long profile. Assessment of post-abandonment tilting of outwash surfaces thus requires comparison to surface profiles outside the zone of tilting and deformation.

[17] We surveyed terrace treads, outwash surfaces, and active channels in each transverse drainage along the Ostler fault using a Trimble 4700 differential GPS with centimeter-level vertical and horizontal precision. This degree of precision is less than the "geomorphic noise," or ground surface irregularities caused by variations in soil or loess cover, generally less than ~10 cm. Scatter in our survey data instead reflects ubiquitous paleochannel rills typically with <1 m of relief on surface treads. Where exposed and accessible for strath terrace surfaces, we also surveyed isolated points along the strath-gravel contact in addition to points along the terrace tread. Additionally, topographic profiles measured from a TOPSAR 10-m digital elevation model were used to supplement our survey coverage. DEM elevations were tied to our survey measurements through repeated surveying of known benchmarks throughout the field area.

2.3. Surface Chronology

[18] Existing radiocarbon, luminescence, and cosmogenic exposure ages in the Mackenzie Basin [*Maizels*, 1989; *Schaefer et al.*, 2001, 2006; *Amos et al.*, 2007] lend support to correlation of the Tekapo and Mount John age divisions with the Last Glacial Maximum (LGM), or Otiran Glacial period in New Zealand [*Suggate*, 1990]. The association of older features with Late Quaternary stratigraphic subdivisions in New Zealand, however, typically relies on tentative correlations to climatic proxies such as the marine isotopic record [e.g., *Martinson et al.*, 1987] or paleoclimatic data from ice cores [*Petit et al.*, 1999]. Actual connections between these records and Quaternary landscape features re-

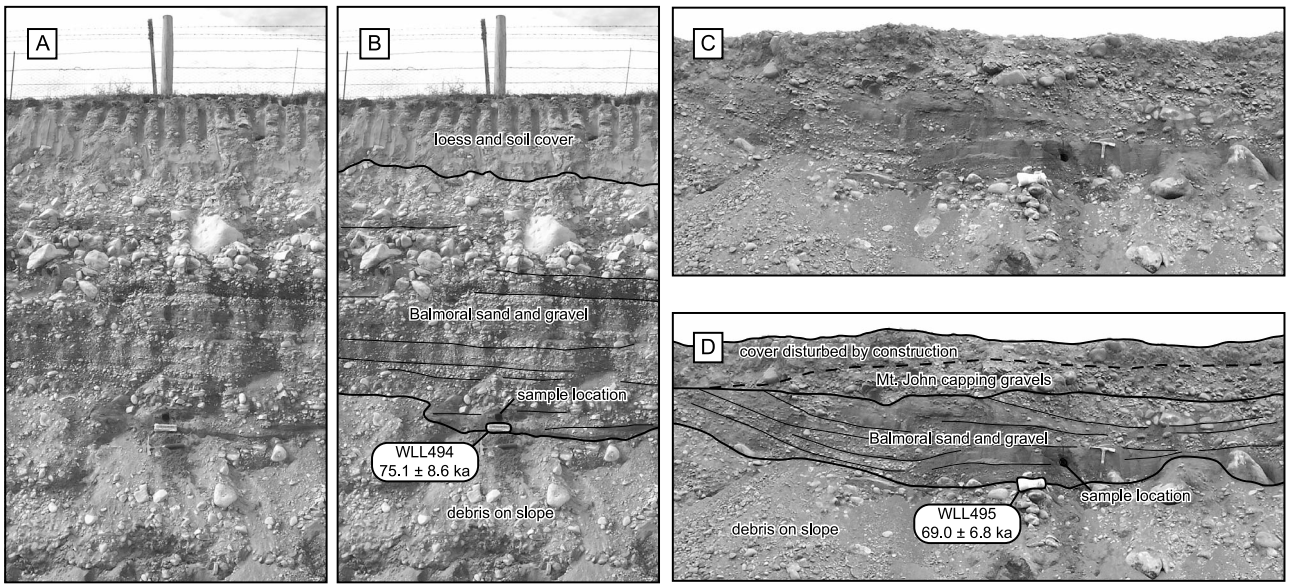

Figure 3. (a) Photograph and (b) interpretation of OSL sample locality WLL494 within terrace fill deposits on a prominent Balmoral outwash terrace. (c) Photo and (d) stratigraphic interpretation of OSL sample locality WLL495, where Mount John capping gravels cover older Balmoral fill below a prominent unconformity. Hammer for scale in each photo.

quire additional geochronologic control beyond the range of radiocarbon dating [*Sutherland et al.*, 2007]. We supplement existing age constraints on geomorphic features in the Mackenzie Basin using optically stimulated luminescence (OSL) dating of terrace sediments and cosmogenic radionuclide dating (CRN) of glacial moraines and outwash surfaces to bracket the timing of terrace formation.

[19] OSL dating of Quaternary sediments can provide accurate constraints on depositional age provided that material was sufficiently exposed to sunlight prior to burial so that its OSL age is reset to zero [*Duller*, 1996; *Aitken*, 1998]. To maximize the likelihood of resetting prior to deposition, we sampled terrace silts and fine sands indicative of overbank deposition in a relatively shallow and quiescent fluvial environment. Our results (Tables 1a and 1b) complement previous luminescence dating of silts beneath Balmoral outwash gravels just north of the Ohau River where it crosses the North Central section of the Ostler fault zone (Figure 1) [*Amos et al.*, 2007]. Those dates indicated a maximum age of ~105 ka and correlation with either marine isotope stage (MIS) 5b or 4. Samples WLL493 and WLL494 (Tables 1a and 1b) represent interbedded sands and silts collected from an exposure into the same Balmoral surface dated in our previous study where it is cut by a prominent scarp along the Haybarn fault section (Figures 1, 3a, and 3b). Although these samples originate from approximately the same stratigraphic interval, their calculated OSL ages differ by ~70 kyr. This age discrepancy may result from the fact that the older of these two samples (WLL493) is likely to be close to saturation, resulting in large data scatter and high error margins (~20%) in the calculated OSL age [U. Rieser, personal communication, 2006]. Incomplete exposure to light prior to burial will also bias samples to older ages. Given that the OSL date for sample WLL493 (143 ± 23 ka, 1σ) is significantly older than the maximum age of two samples from beneath the terrace gravels (~105 ka) [*Amos et al.*, 2007], we use only the younger sample age of 75.1 ± 8.6 ka (1σ, WLL494) as a minimum constraint on the Balmoral T2 terrace (Figure 2).

[20] Samples WLL495 and WLL496 also represent interbedded sand and silt collected from Balmoral outwash gravels (Figures 3c and 3d). These ages, 69.0 ± 6.8 and 72.9 ±

Table 1a. Luminescence Dating Results: Water and Radionuclide Contents

Sample Number[a]	Location (Latitude/Longitude)	Altitude (m)	Sample Depth (m)	Water Content δ[b]	U (μg/g) From ^{234}Th	U (μg/g) From ^{226}Ra, ^{214}Pb, ^{214}Bi[c]	U (μg/g) From ^{210}Pb	Th (μg/g) From ^{208}Tl, ^{212}Pb, ^{228}Ac[c]
WLL493	−44.23887°/170.02568°	561	3.4	1.192	2.66 ± 0.26	2.62 ± 0.17	2.70 ± 0.24	10.5 ± 0.13
WLL494	−44.23881°/170.02582°	556	3.15	1.144	3.08 ± 0.30	2.84 ± 0.19	2.94 ± 0.26	10.88 ± 0.15
WLL495	−44.26513°/170.04730°	526	1.3	1.078	2.03 ± 0.25	2.21 ± 0.16	2.45 ± 0.23	9.72 ± 0.13
WLL496	−44.26527°/170.04723°	526	0.85	1.092	2.07 ± 0.26	2.12 ± 0.17	2.36 ± 0.23	9.76 ± 0.13

[a]Sample preparation and measurements at the Luminescence Dating Laboratory, School of Earth Sciences, Victoria University, Wellington, NZ.
[b]Ratio wet sample to dry sample weight. Errors assumed 50% (δ-1).
[c]U and Th-content is calculated from the error weighted mean of the isotope equivalent contents.

Table 1b. Luminescence Dating Results: Measured K Content, α-Value and Equivalent Dose, Cosmic Dose Rate, Total Doserate, and OSL Age

Sample Number[a]	K (%)	Alpha Effectiveness α-Value[b]	Equivalent Dose, D_e (Gy)	dD_e/dt (Gy/ka)[c]	Dose Rate dD/dt (Gy/ka)	OSL-age (ka) and 1σ Uncertainty[d]	Age Association[e]	Field Code
WLL493	2.15 ± 0.05	*0.05 ± 0.02*	535.7 ± 76.2	0.1448 ± 0.0072	3.75 ± 0.30	142.7 ± 23.3	Balmoral	HBOSL-05-02
WLL494	2.03 ± 0.05	*0.07 ± 0.03*	312 ± 21.5	0.1495 ± 0.0075	4.16 ± 0.38	75.1 ± 8.6	Balmoral	HBOSL-05-03
WLL495	1.99 ± 0.04	0.117 ± 0.015	314.3 ± 27.6	0.1911 ± 0.0096	4.56 ± 0.20	69.0 ± 6.8	Balmoral	EROSL-05-01
WLL496	2.02 ± 0.04	0.073 ± 0.009	296.8 ± 10.1	0.2033 ± 0.0102	4.07 ± 0.16	72.9 ± 3.8	Balmoral	EROSL-05-02

[a]Sample preparation and measurements at the Luminescence Dating Laboratory, School of Earth Sciences, Victoria University, Welllington, NZ.
[b]Italics indicate an estimated α–value due to saturation of the α–irradiated subsample.
[c]Contribution of cosmic radiation to the total doserate, calculated as proposed by *Prescott and Hutton* [1994].
[d]Sample WLL493 was close to saturation and the large error margins reflect difficulties in fitting data points (U. Rieser, personal communication, 2006).
[e]Age designation based on previously defined Quaternary chronologies. See text for discussion.

3.8 ka (1σ), respectively, are indistinguishable from sample WLL494 at 95% confidence, and they further support a minimum Balmoral age of 70–75 ka (Tables 1a and 1b). Samples WLL495 and WLL496, however, originate from an outwash exposure beneath a prominent Mount John outwash terrace (Figures 3c and 3d). Whereas the minimum Balmoral age from the Haybarn scarp to the northwest (WLL494) comes from above a bedrock strath with < 10 m of gravel cover, the presence of older fill beneath Mount John terrace gravels suggests a significant southward thickening of Balmoral outwash in the Ohau River valley (Figure 4). Overlap among these three minimum ages also suggests synchrony between the deposition of terrace gravels and outwash accumulation during creation of the Balmoral T2 terrace.

[21] Weighted averages of OSL dates presented here and in our previous study [*Amos et al.*, 2007, Table 1b] bracket formation of the Balmoral strath between 72.4 ± 3.1 and 104.9 ± 6.3 ka (1σ), respectively. Comparison with paleoclimatic proxy records reveals atmospheric cooling in the southern hemisphere during this time [*Petit et al.*, 1999] and further supports correlation of Balmoral terraces with MIS 5b or early stage 4 (Figure 2). This period also overlaps with the timing of widespread glacial advance recognized throughout New Zealand, culminating at ~80 ka [*Preusser et al.*, 2005; *Sutherland et al.*, 2007].

[22] Geochronologic constraints on both the Wolds and Tekapo surfaces come from CRN exposure-age dating of boulders and cobbles preserved on these landforms. Exposure-age dates were calculated by measuring cosmogenic ^{10}Be present in quartz extracted from Torlesse metasedimentary rocks deposited on end moraines and outwash surfaces. For glacial moraines, we sampled the uppermost surface of the largest boulders, typically >1 m in diameter for the youngest moraines, present near the terminal moraine crest. Samples collected from outwash surfaces include both the largest individual cobbles present and an amalgam of surface chips from ~10 additional cobbles of metagreywacke. The resulting exposure ages (Table 2) were computed using the CRONUS-Earth online exposure age calculator, Version 2.2, as described by *Balco et al.* [2008] using the scaling scheme or spallation of *Lal* [1991] and

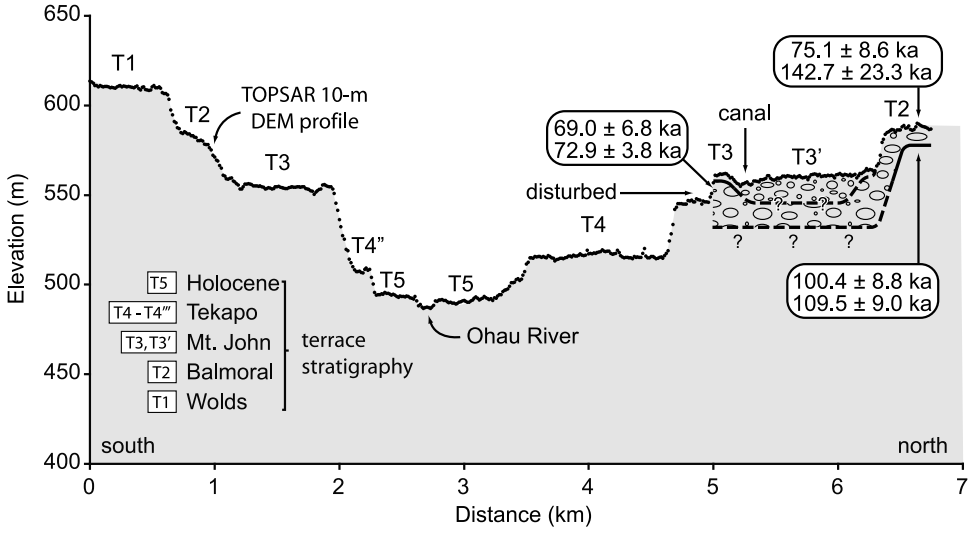

Figure 4. Topographic profile across the Ohau River Valley from the TOPSAR 10-m DEM showing the general pattern of older surfaces stepping down in elevation to the modern channel. The profile location is shown on Figure 1.

Table 2. Analytical Results of 10Be Geochronology

Sample[a]	Sample Type	Location (Latitude/Longitude)	Altitude (m)	Quartz[b] (g)	Sample Thickness (cm)	Topographic Shielding Factor	Be Carrier[c] (mg)	^{10}Be/Total Be (10^{-12})	Measured ^{10}Be[d] (10^6 atoms/g SiO_2)	^{10}Be Model Age[e] (ky)	Age Association[f]
OSTCRN-304-1	moraine	−44.38601°/169.94792°	585	24.7303	5	0.99978	0.3017	0.853 ± 0.039	0.680 ± 0.032	84.8 ± 8.6	Wolds
OSTCRN-304-2	moraine	−44.38706°/169.94756°	582	18.6288	5	0.99978	0.2978	0.359 ± 0.017	0.362 ± 0.019	44.9 ± 4.6	Wolds
OSTCRN-304-3	moraine	−44.38857°/169.94798°	585	27.5389	5	0.99978	0.2986	0.782 ± 0.098	0.552 ± 0.071	68.6 ± 10.8	Wolds
OSTCRN-304-4	moraine	−44.38765°/169.94887°	588	22.0906	5	0.99978	0.2990	0.776 ± 0.040	0.683 ± 0.036	85.1 ± 8.8	Wolds
OSTCRN-304-5	moraine	−44.38634°/169.94893°	578	11.8846	5	0.99978	0.3013	0.297 ± 0.024	0.469 ± 0.041	58.5 ± 7.3	Wolds
TMMM-05-01	moraine	−44.10312°/170.05282°	838	27.3494	5	0.99760	0.2983	0.217 ± 0.019	0.144 ± 0.014	14.4 ± 1.9	Tekapo
TMMM-05-02	moraine	−44.10242°/170.05339°	842	39.4435	5	0.99760	0.2923	0.271 ± 0.027	0.125 ± 0.013	12.4 ± 1.7	Tekapo
TMMM-05-03	moraine	−44.10273°/170.05340°	839	34.5118	5	0.99760	0.2948	0.297 ± 0.029	0.158 ± 0.017	15.9 ± 2.2	Tekapo
TMMM-05-04	moraine	−44.10446°/170.05153°	826	57.0348	5	0.99690	0.2994	0.532 ± 0.020	0.180 ± 0.007	18.2 ± 1.7	Tekapo
OSTCRN-224-1	clast	−44.15680°/170.02949°	750	29.7511	3	0.99872	0.2970	1.093 ± 0.065	0.716 ± 0.043	76.9 ± 8.3	Wolds
OSTCRN-224-2	clast	−44.15755°/170.03074°	750	37.0946	3	0.99872	0.2981	1.745 ± 0.066	0.927 ± 0.036	100.0 ± 9.7	Wolds
OSTCRN-224-3	clast	−44.15588°/170.03062°	750	51.8916	3	0.99872	0.3009	2.943 ± 0.119	1.133 ± 0.046	122.9 ± 12.1	Wolds
OSTCRN-224-6	clast amalgam	−44.157°/170.030°	750	22.6297	3	0.99872	0.2988	1.167 ± 0.075	1.012 ± 0.066	109.5 ± 12.2	Wolds

[a]Samples prepared and measured at the PRIME Lab, Purdue University, West Lafayette, IN.
[b]Exposure age calculations employ a sample density of 2.7 g/cm^3 for all samples.
[c]Be carrier concentration is 1.45 mg/g.
[d]Propagated uncertainties include errors in the blank, carrier, and counting statistics.
[e]Model ages and uncertainties calculated using the CHRONUS-Earth online calculator (Version 2; http://hess.ess.washington.edu/) [*Balco et al.*, 2008], using the scaling scheme for spallation from *Lal* [1991] and *Stone* [2000].
[f]Age designation based on previously defined Quaternary chronologies. See text for discussion.

Stone [2000]. All model exposure ages assume zero boulder and clast erosion.

[23] Exposure ages calculated for five boulder samples from a prominent Wolds end moraine at Willowbank saddle (OSTCRN-304-1 through 5) exhibit substantial scatter, ranging between ~45 and 85 ka (Table 2). A composite probability density function of these ages (Figure 5a) reveals little overlap among individual ages and suggests that these samples reflect diminution of cosmogenic ^{10}Be through post-depositional erosion. The smooth, relatively subdued geomorphic surface appearance of this moraine and the scarcity of large boulders protruding through the regolith cover are consistent with substantial diffusive erosion of the moraine crest and some combination of exhumation and surface erosion of the constituent boulders. As such, we discount these ages in our assessment of the timing of the Wolds glaciation and surface formation.

[24] In contrast, CRN exposure ages calculated for four boulder samples from a relatively fresh and rocky Tekapo end moraine preserved on the northern section of the Ostler fault at Top McMillan Stream (TMMM-05-1 through 4) cluster between ~12 and 18 ka and overlap well within 2σ uncertainties (Table 2). A composite probability density function of these ages exhibits a strong peak at 15.2 ± 2.4 ka (Figure 5b), suggesting minimal post-depositional erosion of these boulders and the moraine crest. The calculated composite peak is in good agreement and only slightly younger than the mean CRN exposure age (17.4 ± 1.0 ka) reported for latest-LGM Tekapo moraines at adjacent Lake Pukaki [*Schaefer et al.*, 2006]. *Schaefer et al.* [2001] also report a CRN exposure age for the oldest LGM Mount John moraines at Lake Pukaki of 26.5 ± 4.0 ka, which stands in good agreement with OSL dating of a prominent Mount John strath terrace along the South Central Ostler fault section [*Amos et al.*, 2007]. Taken together, these dates suggest an ~10 kyr duration for the LGM within the Lake Pukaki Valley [*Schaefer et al.*, 2001].

[25] Samples OSTCRN-224-1, 2, 3, and 6 originate from intact cobbles preserved on a prominent Wolds T1 strath terrace surface at Dry Stream, preserved between the Northern and Haybarn fault sections (Figure 1). Calculated CRN exposure ages for these samples range between ~77 and 123 ka (Table 2) with an apparent age cluster near the older (>100 ka) range of the total age spectrum for these samples. Bias toward younger ages evident in the age spectrum at Dry Stream (e.g., OSTCRN-224-1, Table 2) indicates a complicated exposure history for these clasts. This exposure history could in part reflect stripping and remobilization of a formerly thick loess cover, which would serve to skew samples to younger ages. Field observations of substantial variation in the thickness of loess blanketing the T1 surface at Dry Stream (of ~1–2 m) suggests the likelihood of this scenario and underscores the CRN ages as a minimum bracket on the timing of Wolds terrace formation. Though we acknowledge the additional possibility of unconstrained bias due to inherited ^{10}Be or a grain-size dependency for our surface-clast samples, we utilize the mean of the three oldest samples at Dry Stream, which form a prominent peak in the total age spectrum (Figure 5c), for this limiting age (110.8 ± 11.5 ka). Taken together, these

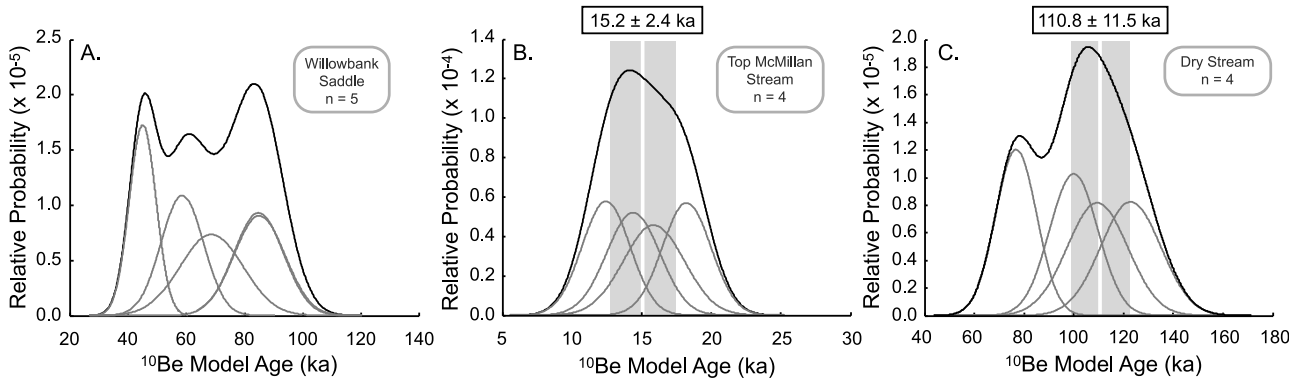

Figure 5. Individual and composite probability density functions for CRN exposure ages for (a) Wolds moraine at Willowbank Saddle, (b) Tekapo moraine at Top McMillan Stream, and (c) a prominent Wolds outwash surface at Dry Stream. Peak ages for the composite curves represent mean ages (vertical white line) and standard errors (gray bars) for all ages at Top McMillan Stream and the three oldest ages at Dry Stream.

exposure ages constrain the timing of the Wolds glaciation to lie within the penultimate glacial maximum, or the Waimea glacial period in New Zealand [*Suggate*, 1990], and suggest potential correlation with MIS 6 (Figure 2).

[26] The general correspondence among terrace ages bracketed here with OSL and CRN exposure dating, climate proxy records, and documented Late-Pleistocene glacial intervals elsewhere in New Zealand [*Suggate*, 1990; *Bull*, 1991; *Preusser et al.*, 2005; *Sutherland et al.*, 2007] lends support to the increasingly widespread recognition that climate exerts fundamental control over fluvial and outwash terrace genesis [e.g., *Bull*, 1991; *Molnar et al.*, 1994; *Pratt et al.*, 2002; *Formento-Trigilio et al.*, 2003; *Litchfield and Berryman*, 2005; *Bookhagen et al.*, 2006]. Climate regulates local variations in sediment supply and discharge that determine both the timing and pattern of lateral erosion and incision during terrace formation [*Hancock and Anderson*, 2002]. Subsequent deformation of terrace and outwash surfaces at the basin scale serves to amplify the effects of regional incision that is ultimately driven tectonic base-level lowering [*Nicol and Campbell*, 2001; *Pan et al.*, 2003; *Bull*, 2007].

3. Deformed Geomorphic Surfaces on the Ostler Fault

3.1. Northern Section

[27] The Northern section of the Ostler fault zone bounds the southeastern margin of the Ben Ohau Range (Figure 1). Along the southern half of this strand, the fault raises Torlesse metasediments in its hanging wall over Quaternary gravels and glacial deposits on the basin floor (Figure 6a). The fault consists of numerous overlapping splays and sections forming a complex, arcuate surface trace with an average trend of ~025°. Northern portions of this fault section cut into the range near the headwaters of the Twizel River and form a prominent bedrock scarp with a quasi-linear surface trace. Farther north, the northern Ostler fault section displaces lateral moraines at Boundary Stream before the active surface trace is buried beneath scree slopes immediately north of Whale Stream. At the southern tip of the Northern section, the surface trace dies out as subtle anticlinal warping of terraces north of Fraser Stream (Figure 6a).

[28] Streams draining the Ben Ohau Range are flanked by flights of Late Quaternary strath terraces that cross the Northern section of the Ostler fault zone. Gravels capping these surfaces are typically less than 1–3 m in thickness. Terrace treads, moraines, fault scarps, and fold axes were mapped using a combination of 1:40,000 and 1:10,000 scale aerial photography (Figure 6). Adjacent terrace treads are separated by risers and display the general pattern of older surfaces stepping down in elevation to younger terraces and the modern river. Strath exposures are relatively continuous along these surfaces and reveal both Kurow Group and Torlesse bedrock (Figure 7). Last-Glacial age terraces (Mount John and Tekapo) predominate toward the northern end of the fault and were identified based on their pristine surface texture and height above the active channel. CRN exposure dating of a prominent terminal moraine at Top McMillan Stream (Figure 5b) aids in differentiating between these two LGM age divisions and in correlating surfaces within adjacent drainages. Widespread aggradation within the footwall of the Northern Ostler fault and from numerous smaller tributary drainages, however, diminishes the certainty of this distinction elsewhere along the Northern fault section (Figure 6a). Nested within the LGM terraces, multiple levels of relatively discontinuous surfaces flank each of the modern streams. We grouped these surfaces as undifferentiated Holocene terraces because the scale of our mapping generally exceeds the size of individual treads in this age range (Figure 6a). Additionally, isolated Balmoral terrace remnants occupy the highest relative positions above Dry and Fraser Stream. Paleochannel rills are generally absent from these Balmoral treads, therefore subduing the overall textural appearance of these relatively older surfaces (Figure 6a). With the exception of active alluvial surfaces flanking the modern channels, the Northern fault section displaces each of the three terrace age groups along its length.

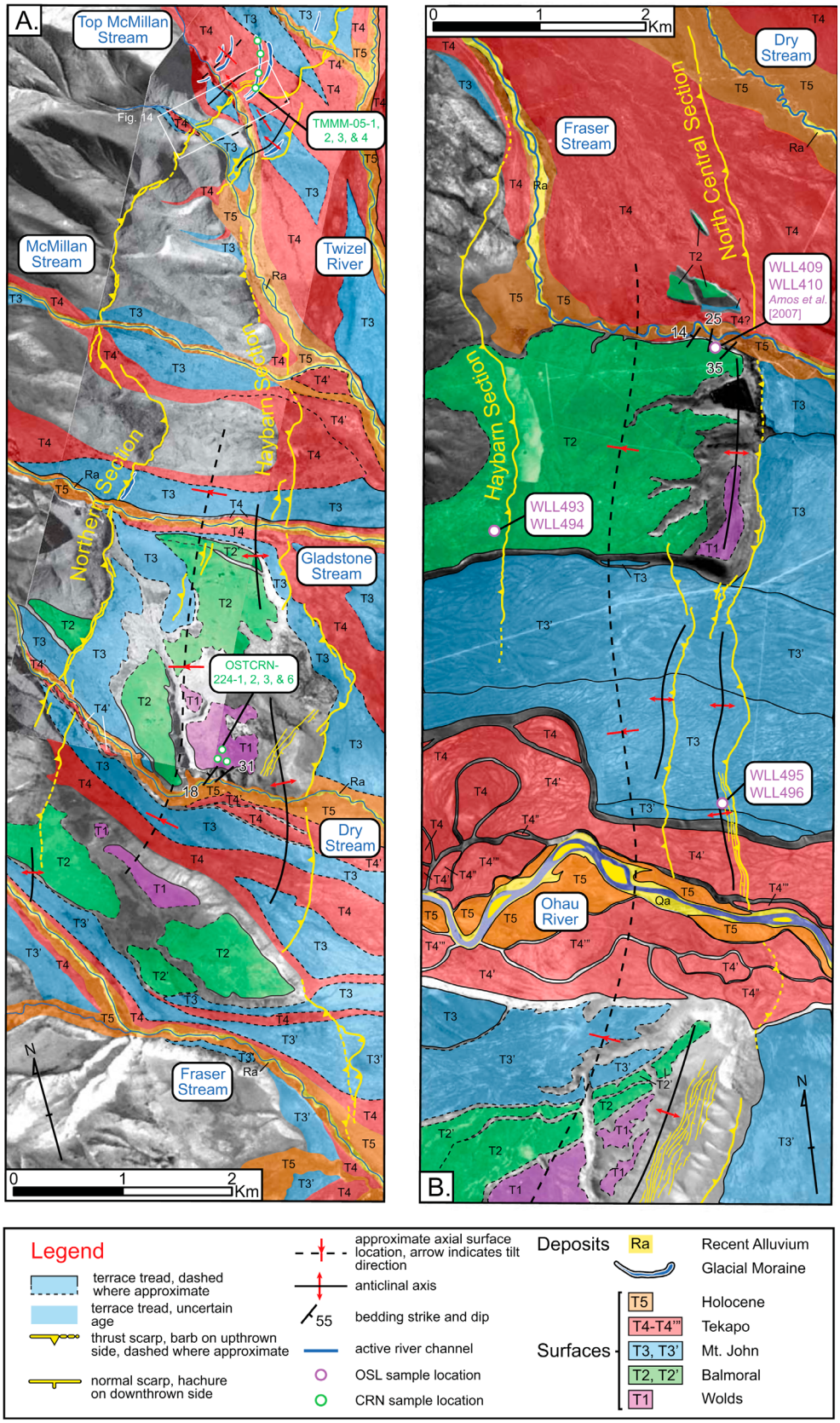

Figure 6. Geomorphic and neotectonic map displaying terrace treads, fault scarps, and fold axes along the (a) Northern and Haybarn and (b) Haybarn and North Central fault sections of the Ostler fault zone.

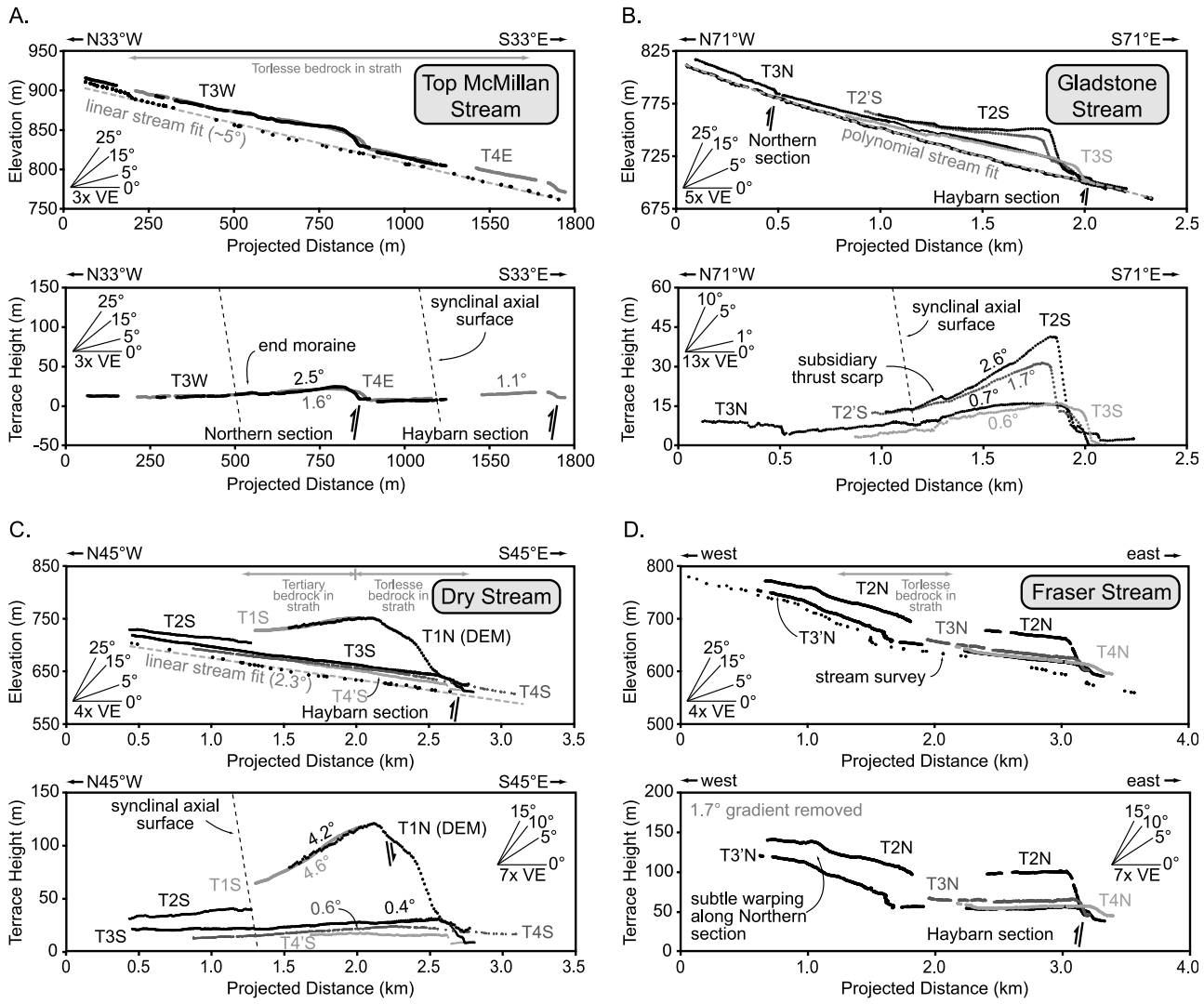

Figure 7. GPS survey profiles of modern channels and deformed strath and outwash terraces preserved along the Northern and Haybarn fault sections. Surveyed points along terrace treads for each terrace level are projected approximately perpendicular to the mapped axial surface orientation. The lower plots for each drainage reflect removal of either a linear or polynomial fit to the modern stream profile (upper plot). Where visible, the bedrock composition in exposed straths is noted along each profile.

[29] Folding along the Northern section exemplifies the two primary styles of hanging wall deformation observed for the Ostler fault zone: uniform uplift with no discernable tilting, and progressive backlimb rotation. Where the Northern section of the Ostler fault zone directly bounds the eastern margin of the Ben Ohau Range (e.g., near Gladstone Stream, Figure 6a), displacement of geomorphic features across the fault generally occurs without significant warping or tilting of terrace treads (see T3N at 0.5 km on Figure 7b). Along Top McMillan Stream, however, the fault trace departs from the range front, and folds are characterized by broad, continuous, and planar backlimbs that grade into flat terrace segments that generally parallel the modern river (Figure 7a). This transition defines an active axial surface [e.g., *Hubert-Ferrari et al.*, 2007] and occurs roughly 300–450 m upstream from the fault trace along a prominent Mount John surface. Folding of this surface is highly asymmetric with a relatively short, steep, and abrupt forelimb and a more extensive and gentler fold backlimb. After removal of the ~5° modern gradient along this reach of Top McMillan Stream, linear regressions through the planar portions folded backlimbs reveal 2.5° and 1.6° westward tilts for the west and east side of Top McMillan stream, respectively (Figure 7a). Removal of a locally linear stream gradient is justified here given the relatively short length of this reach and the overall parallelism of untilted terrace segments and the stream-profile regression.

3.2. Haybarn Section

[30] The Haybarn section of the Ostler fault zone [*Read*, 1984; *Blick et al.*, 1989] sits east of the Northern fault

section along the southeast margin of the Ben Ohau Range (Figure 1). Unlike the Northern section, however, the Haybarn fault cuts basin deposits along much of its length and reveals both Kurow bedrock and Torlesse basement rocks in hanging wall strath exposures (Figures 6a and 7). Where exposed, Kurow beds north of Dry Stream display exclusively westward dips of ~20–30°NW (Figure 6a). The surface trace of the Haybarn fault is also relatively complex with numerous splays and overlapping step-overs suggestive of slip transfer among individual fault segments [*Davis et al.*, 2005]. Numerous, subparallel normal fault scarps immediately north of Dry Stream (Figure 6a) also indicate localized extension and topographic collapse of the uplifted hanging wall [*Eusden et al.*, 2003] along portions of the Haybarn fault. To the north, the Haybarn section tips out near its intersection with the Northern section of the Ostler fault zone west of the Twizel River (Figure 5a). The Haybarn fault terminates at its southern end along a prominent Mount John outwash surface just north of the Ohau River (Figure 6b).

[31] Geomorphic surfaces mapped on 1:40,000 and 1:10,000 scale aerial photographs across the Haybarn fault also reveal the general pattern of strath terraces stepping down in elevation to younger terraces and the modern river (Figures 6a and 6b). Like the Northern section, the Haybarn fault cuts surfaces of each age designation, except the modern channel alluvium. Exposed straths reveal both Torlesse and Kurow bedrock beneath ~1–3 m of capping gravel, and many terrace surfaces are continuous across both the Haybarn and Northern fault sections (Figure 7). Surfaces to the east, however, may be largely aggradational in the footwall of the Haybarn fault. OSL ages (WLL493 and 494, Tables 1a and 1b) from the prominent T2 outwash terrace cut by the southern Haybarn section (Figure 6b) confirm correlation of this surface with the Balmoral age association (Figure 2). Additionally, several older, isolated strath terrace remnants occupy the highest relative positions above Dry and Fraser Streams (Figure 6b). The aforementioned CRN exposure dating of the broad T1 terrace immediately north of Dry Stream confirms its correlation with the Wolds age division (Figure 5c).

[32] Folded terraces along northern sections of the Haybarn fault also display the general pattern of broadly west-tilted fold backlimbs and abrupt, east-dipping forelimbs (Figure 7). Across the synclinal axial surface bounding each fold backlimb, untilted terrace segments in the hanging wall flatten and trend parallel to the modern river profile. This deformation pattern mimics folds across the Northern fault section for the Tekapo surface at Top McMillan Stream, where removal of the ~5° stream gradient reveals a moderate, 1.1° westward tilt upstream of the Haybarn fault (Figure 7a). Where multiple generations of surfaces are preserved across the fault, deformed treads show continuously greater tilts for older terrace generations (Figure 7). Terraces profiles at Gladstone Stream exemplify this pattern of progressive backlimb rotation, and removal of a polynomial fit to the modern stream uncovers a 2.6° and 1.7° westward tilt for the Balmoral T2 and T2′ surfaces, respectively (Figure 7b). Younger, Mount John straths on either side of Gladstone Stream display more modest 0.6° and 0.7° backlimb tilts. To the south, older Wolds strath terrace remnants preserved along the flanks of Dry Stream (Figure 5a) display even greater degrees of westward backlimb tilting between 4.2° and 4.6° after removal of a linear fit to the channel profile (Figure 7c). Folded backlimbs along Mount John and Tekapo surfaces adjacent to Dry Stream show slight westward tilts across the synclinal axial surface of 0.4–0.6° (T3 and T4, respectively), whereas the youngest Tekapo T4′ terrace roughly parallels the linear stream profile along its length (Figure 7c). Greater tilts on the inset T4 surface compared to the older T3 terrace at Dry Stream suggest either a lower limit on our ability to resolve small amplitude tilting or an along-strike increase in backlimb rotation to the south.

[33] Terrace deformation patterns along southern portions of the Haybarn section change markedly where the Northern fault terminates and the Haybarn fault takes over as the bounding thrust for the Ben Ohau Range (Figures 1 and 6). As evident along Fraser Stream, deformed strath terrace treads display little discernible tilting after removing a 1.7°, linear streamwise gradient from surveyed terrace profiles (Figure 7d). Instead, differential uplift across the Haybarn fault appears to be broadly uniform and occurs without the downstream divergence of progressively older terrace treads characteristic of folded surfaces outboard of the main range front to the north (Figure 7d). We use a streamwise reference gradient measured along the thalweg of Fraser Stream because of the overall complexity of the channel profile when projected perpendicular to the N–S fault strike in this location.

3.3. Central Sections

[34] Central sections of the Ostler fault zone extend for ~40 km from north of the Ohau River to the Ahuriri River in the south (Figure 1). A prominent, ~1 km step-over or relay ramp at Willowbank Saddle separates the Central section into the ~015° trending North Central strand and the more northeasterly trending (~025°) South Central portion of the Ostler fault zone. Both fault sections bound a series of low hills to the west composed of Plio-Pleistocene Kurow Group strata. Bedding orientations within these uplifted blocks also display exclusively westward dips of ~25–55°NW (Figures 6b and 8b). Like other sections of the Ostler fault, surface traces within both the North Central and South Central sections are complex and include: numerous synthetic, en echelon thrust scarps and splays; several prominent west-directed backthrusts; and abundant normal fault scarplets accommodating localized hanging wall extension and crestal graben formation [e.g., *Bull*, 2007, Figure 1.10] (Figures 6b and 8). Several such normal faults north of Quailburn (Figure 8b) display down-to-the-west displacements and appear to follow west-dipping bedding within the Tertiary sequence. The overall surface trace of the Central Ostler fault sections generally decreases in complexity to the south, where the South Central section completes a 90° change in strike and terminates to the west along the Ahuriri River (Figure 1). This section of the Ostler fault zone is termed "the knot" and described in detail by *Read and Blick* [1991].

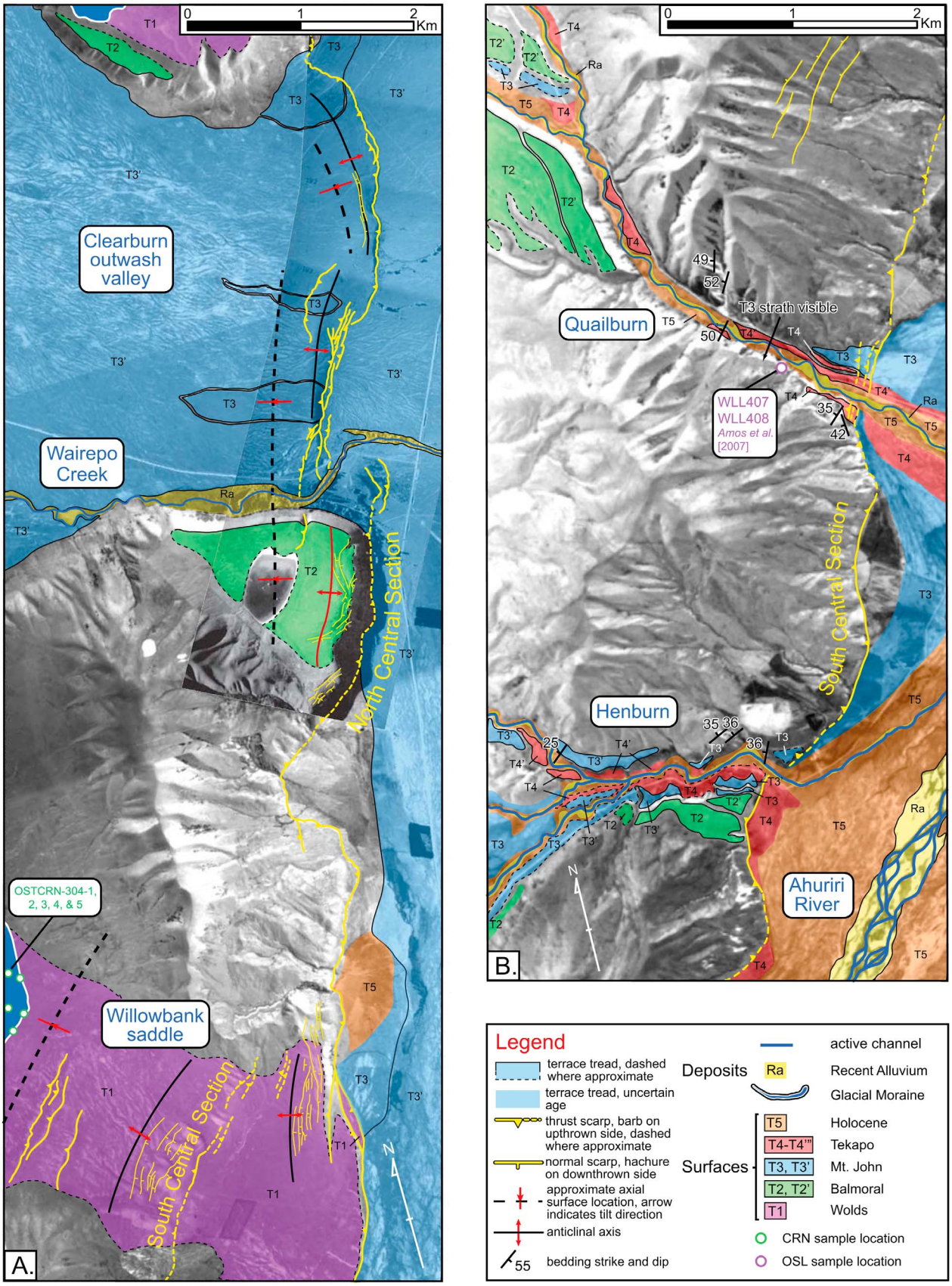
0 1 2 Km
Clearburn outwash valley
Wairepo Creek
North Central Section
South Central Section
OSTCRN-304-1, 2, 3, 4, & 5
Willowbank saddle
A.
Quailburn
T3 strath visible
WLL407
WLL408
Amos et al. [2007]
Henburn
Ahuriri River
B.
Legend
terrace tread, dashed where approximate
terrace tread, uncertain age
thrust scarp, barb on upthrown side, dashed where approximate
normal scarp, hachure on downthrown side
approximate axial surface location, arrow indicates tilt direction
anticlinal axis
bedding strike and dip
Deposits
active channel
Recent Alluvium
Glacial Moraine
Surfaces
Holocene
Tekapo
Mt. John
Balmoral
Wolds
CRN sample location
OSL sample location

Figure 8

[35] Mapping of transverse drainages using 1:40,000 and 1:10,000 scale aerial photographs reveals multiple generations of deformed outwash and strath terraces across both the North and South Central sections of the Ostler fault zone (Figures 6b and 8). Along the North Central Ostler fault, outwash terraces predominate. Strath terraces revealing the underlying Kurow bedrock are more common along the South Central section, although outwash terraces are also present. Where active drainage continues across the fault, terrace surfaces display the general pattern of older surfaces stepping down in elevation to younger terrace treads and the modern river channel. Flights of outwash, strath, and cut terraces along the Ohau River exemplify this relationship and reveal a nearly complete sequence of Mackenzie Basin surfaces from the high Wolds strath terraces to the younger, Holocene surfaces (Figures 4 and 6b).

[36] Deformed terrace surfaces within two broad paleo-outwash valleys, now preserved as wind gaps, record the progressive defeat of formerly transverse drainage along the Central Ostler fault zone. Correlation of these outwash surfaces with the Mount John and Wolds age divisions suggests minimum ages on the Clearburn outwash valley and Willowbank saddle of ~26 ka [*Schaefer et al.*, 2001; *Amos et al.*, 2007] and >120 ka [*Read*, 1984], respectively (Figure 8a). The last-glacial-age outwash surface at Clearburn, T3′ (Figure 8a), is also continuous to the north with Mount John surfaces flanking the Ohau River, where both the younger Tekapo outwash terrace and modern drainage continue across the North Central fault section. Continuity between these terraces implies that active outwash occupied both the Clearburn and Ohau River valleys during Mount John time. The footwall is largely aggradational along the Central Ostler fault section and is blanketed by Mount John outwash for much of its length (Figure 8). Footwall aggradation from both Tekapo and Mount John outwash fans also occurs at the Quailburn drainage, and Holocene and younger gravels of the Ahuriri River cover much of the footwall at Henburn (Figure 8b). Aside from the youngest Holocene surfaces and recently active channel alluvium (Figure 5b), central sections of the Ostler fault zone generally cut all terrace levels of Tekapo age and older.

[37] Like the Haybarn fault, styles and patterns of terrace deformation change markedly along strike for central sections of the Ostler fault zone. Folded outwash surfaces along the Ohau River (Figure 6b) display progressively increasing westward tilts for older terrace treads (Figure 9a), similar in character to folds observed along the northern Haybarn fault. Originally described in our earlier study [*Amos et al.*, 2007], survey profiles along the northern and southern margins of the prominent Balmoral outwash terrace north of the Ohau River (Figure 6b) reveal backlimb tilting between 4.3° and 2.4°, respectively, after removing the linear 0.4° river gradient along this reach (Figure 9a). The gradient along this short reach lies parallels to untilted portions of the Mount John outwash terrace and thus is interpreted to approximate the original slope of these surfaces during deposition. Greater degrees of observed backlimb tilting on the Tekapo outwash surface (1.1°) versus the Mount John tread (0.8°) in this location may represent a lower limit on our ability to resolve small amplitude folding or an along-strike change in slip rate or fault geometry.

[38] Folded outwash terraces at both Clearburn and Willowbank saddle display similar surface deformation patterns to those observed for the Ohau River surfaces. In each location, surface profiles reveal strongly asymmetric anticlines with extensive and smoothly continuous, west-tilted backlimbs, and relatively short, steeper, east-dipping forelimbs (Figures 9b and 9c). Measurement of backlimb tilting for surfaces contained within these wind gaps, however, requires comparison to surface gradients outside the zone of active folding, because modern drainage is either entirely blocked or tectonically perturbed. Wairepo Creek, the small underfit stream flowing across the Clearburn saddle, displays a prominent knickpoint along the modern profile as it crosses the North Central strand of the Ostler fault (Figure 9b). The catchment for Wairepo Creek is at least an order of magnitude smaller than the river system responsible for creating the abandoned outwash surfaces. The warped reach of Wairepo Creek departs from both channel gradients and outwash surface slopes upstream of the area affected by folding (0.3°). As such, we subtract this unperturbed, upstream slope from Clearburn outwash terrace profiles to obtain westward tilts of 3.9°, 1.4°, and 1.1° from regressions through the T2, T3, and T3′ backlimbs, respectively (Figure 9b). For the Wolds T1 outwash terrace at Willowbank saddle, removal of a linear 0.3° surface gradient measured upstream of the active fold suggests backlimb tilting of 3.0–3.3° along the western fold above the South Central fault section (Figure 9c). Backlimb regressions through this surface across the frontal fold yield 1.7–2.3° westward tilts. Overall parallelism between survey profiles outside the zone of active folding and untilted outwash terrace segments (Figures 9b and 9c) suggests that reach-scale surface profiles during deposition were approximately linear in both the Clearburn and Willowbank outwash valleys.

[39] To the south, terrace profiles measured along Quailburn (Figure 8b) also show progressive tilting of older surfaces, although a lack of surface continuity along this drainage prevents measurement of fold geometries across the entire structure (Figure 9d). A prominent Mount John strath terrace (T3) with a minimum OSL age of 27–40 ka [*Amos et al.*, 2007] also appears to gradually roll over the fold forelimb, implying an overall geometry with significantly less asymmetry than observed to the north. Displaced geomorphic surfaces at Henburn, however, do not exhibit any significant warping or tilting across the South Central fault section (Figure 9e). Similar to terrace profiles at Fraser Stream (Figure 7d), terrace deformation at Henburn consists of broadly uniform, differential uplift of terrace treads that parallel the modern, 0.9° linear stream gradient. Survey

Figure 8. Geomorphic and neotectonic map displaying terrace treads, fault scarps, and fold axes along the (a) North Central and (b) South Central fault sections of the Ostler fault zone. Aside from Wairepo Creek, active drainage is diverted northward from the paleo-outwash valleys at Willowbank Saddle and Clearburn.

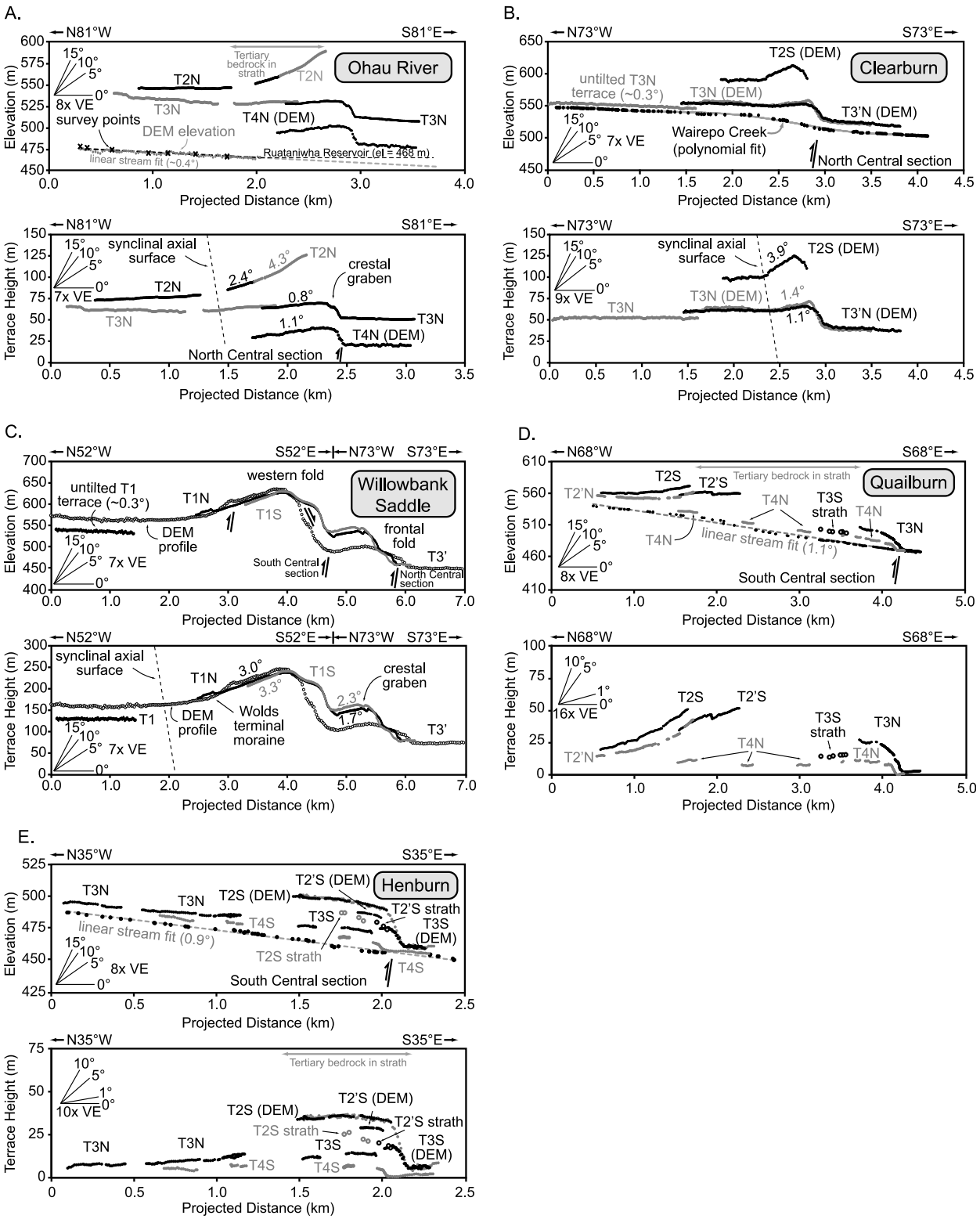

Figure 9. GPS survey profiles of modern channels and deformed strath terraces and outwash surfaces preserved along the central Ostler fault zone. Surveyed points along terrace treads for each terrace level are projected approximately perpendicular to the mapped axial surface orientation. The lower plots for each drainage reflect removal of a linear or polynomial fit to modern stream profile points or untilted surfaces upstream of the deformation zone (upper plot). Where visible, the bedrock composition in exposed straths is noted along each profile.

measurements along exposed portions of the Balmoral T2 and T2′ straths imply some degree of eastward rollover at the fold forelimb, although the measured terrace treads remain roughly planar downstream.

4. Fault Displacement, Slip Rate, and Subsurface Fault Geometry Predictions

4.1. Scarp Profiling and Kinematic Modeling

[40] The combined results of our geomorphic mapping, topographic surveying, and terrace dating allow calculations of fault slip and slip rate for individual profiles of deformed geomorphic surfaces along the Ostler fault zone. Where a terrace is continuous and displaced vertically over the surface trace of an active thrust, survey profiling across the fault scarp provides a straightforward means for estimating the total surface displacement (Figure 10a). We use the approach developed by *Thompson et al.* [2002] for calculating fault slip from regression parameters fit to survey points along the hanging wall tread, scarp face, and footwall tread (Figure 10a). Surface gradients for a displaced terrace often differ slightly on either side of the fault, thus making calculations of total displacement a function of the regression slopes and intercepts, fault dip, and the intersection position of the fault plane with the scarp face. Survey profiles were collected across scarps where scarp erosion has been relatively minimal (e.g., Figure 10a), and regressions through the hanging wall and footwall slopes only include points along intact portions of the terrace tread on either side of the scarp.

[41] Where geomorphic surfaces are discontinuous across an active fault scarp or preserved only in the hanging wall, displacement estimates require matching observed deformed terrace geometries to the predictions of combined geometric and kinematic models for thrust-related folding [e.g., *Lavé and Avouac*, 2000; *Thompson et al.*, 2002]. Like growth strata [*Suppe et al.*, 1992], geomorphic surfaces have long been recognized as faithful recorders of surface folding as slip accumulates on the underlying thrust [e.g., *Rockwell et al.*, 1984; *Stein and King*, 1984]. As such, the presence of multiple surface generations preserved across an active fault-related fold can provide a unique signature of deformational style and aids in identifying the appropriate kinematic model for characterizing a given structure [e.g., *Gold et al.*, 2006; *Scharer et al.*, 2006; *Amos et al.*, 2007; *Hubert-Ferrari et al.*, 2007; *Simoes et al.*, 2007].

[42] An earlier study [*Amos et al.*, 2007] demonstrated that the broad, smoothly continuous and progressively tilted backlimbs observed for folded terraces along the Ostler fault zone are consistent with deformation over a curved or listric thrust ramp at depth (Figure 10b). In this model, accumulation of slip along an emergent, listric thrust fault results in progressive limb rotation and the development of asymmetric hanging wall anticlines [*Erslev*, 1986; *Seeber and Sorlien*, 2000; *Abdrakhmatov et al.*, 2001; *Amos et al.*, 2007]. In contrast with other kinematic models involving limb rotation, such as detachment folding [*Hardy and Poblet*, 1994; *Poblet and McClay*, 1996; *Scharer et al.*, 2006] or shear fault-bend folding [*Suppe et al.*, 2004; *Hardy and Connors*, 2006], differential uplift, when occurring above a listric thrust with constant curvature, varies smoothly as a function of distance along the fault ramp [*Pinter et al.*, 2001], and folding occurs without the development of angular kinks in terrace treads. If the listric fault merges tangentially into a planar ramp at depth (Figure 10b), deformed terraces will display a transition across the synclinal axial surface from uniform differential uplift above the planar ramp to increasing backlimb tilts over the listric fault segment. Terrace segments outside the zone of tilting are offset vertically but remain roughly parallel with untilted footwall surfaces.

[43] Terrace profiling through the transverse drainages across each section of the Ostler fault zone reveals fold geometries compatible with deformation over both listric and planar thrust ramps (Figures 7 and 9). Because we are largely concerned with the magnitude of differential tilting and uplift of terrace surfaces directly across the Ostler fault zone, our approach contrasts with comparisons among strath heights as a proxy for regional, tectonically driven downcutting [e.g., *Bull*, 2007]. As such, folding of both strath and outwash terrace surfaces provides an ideal means for quantifying fault displacement, provided that the initial geometry of these landforms can be reasonably approximated.

[44] For areas consistent with listric thrusting, we follow the methodology outlined by *Amos et al.* [2007] for calculating displacements from progressive tilts of individual terrace surfaces. In this model, fault slip is approximated by rigid rotation over a circular arc and is directly proportional to the observed degree of backlimb tilting (Figure 10b). Displacement then is a simple function of the tilt angle, as determined by regression through the survey data and the radius of curvature, which can be calculated from the measured width of backlimb tilting and the shallow subsurface fault dip [*Erslev*, 1986; *Seeber and Sorlien*, 2000].

[45] Abrupt and narrow forelimbs form in this model by extension and collapse of the hanging wall as it rides over the free surface of the undeformed footwall. Uplift of material over this free surface is analogous to the decrease in

Figure 10. Geometric/kinematic analysis of deformed terraces for (a) individual fault scarps and (b) folded terrace profiles. For scarps, displacement is calculated from vertical separations given by regression parameters through the hanging wall, scarp face, and footwall tread; fault dip; and the position of the fault plane along the scarp face. Folded terraces yield displacement estimates from measured backlimb tilting, fault dip in the shallow subsurface, and the radius of fault curvature. Continuity of slip across the synclinal axial surface results in differential uplift, *dz*, of the untilted terrace tread equal to the magnitude of slip times the sine of the ramp dip at depth. (c) Schematic illustration of inputs for Monte Carlo calculation of fault parameters and associated uncertainties. Reported values of fault slip-rate, displacement, and fault geometry reflect the mode and 95% confidence intervals of the output histograms.

fault dip expected due to footwall collapse driven by progressive loading of the fault plane [*Seeber and Sorlien*, 2000]. In either case, creation of a locally convex ramp in the shallow subsurface results in the development of a narrow fold forelimb despite an overall lack of updip fault propagation. Internal deformation of the hanging wall can occur as subsidiary faulting within the tilted backlimb or through layer-parallel shear as a means for conserving bed

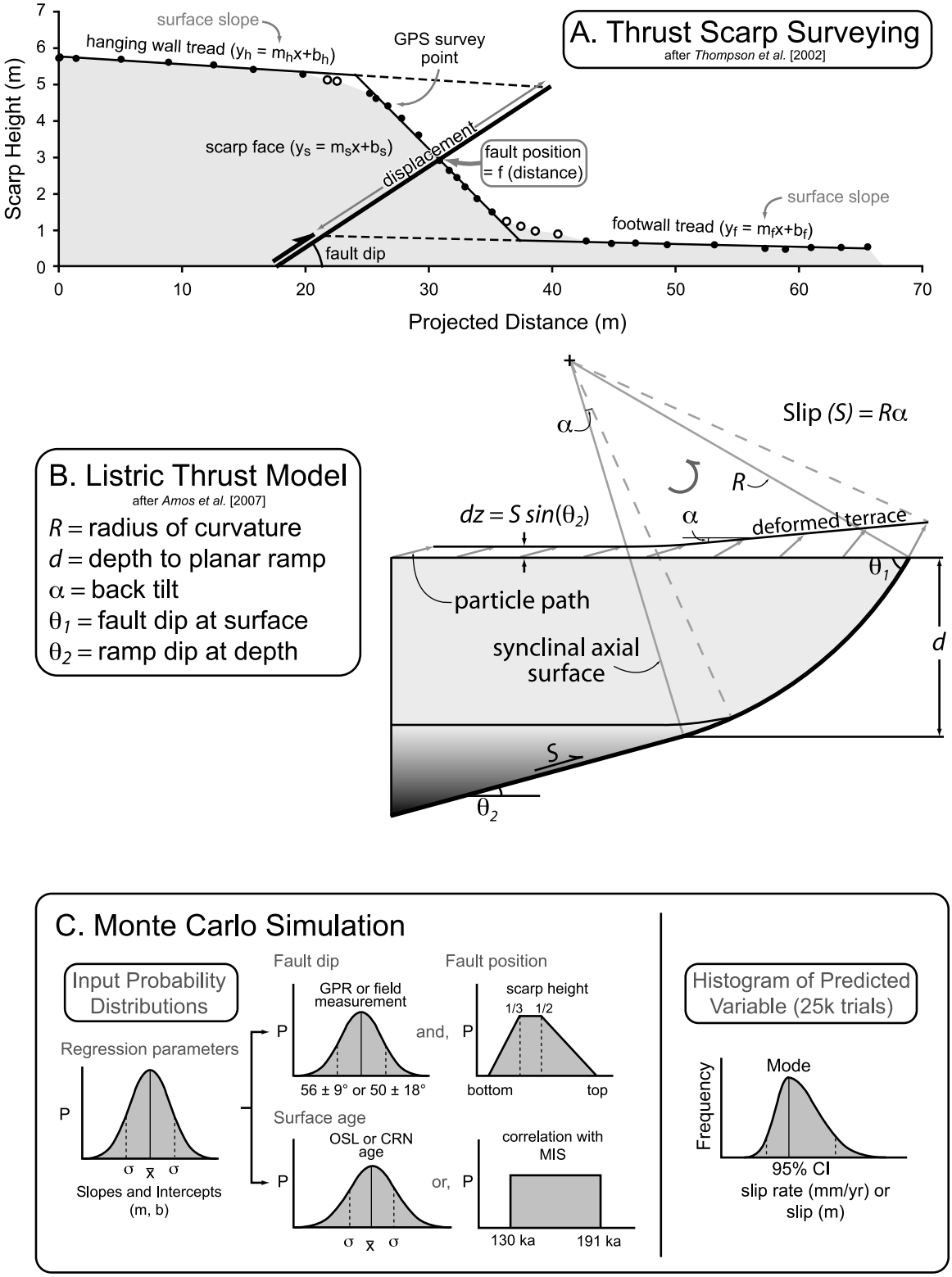

Figure 10

length [*Bulnes and McClay*, 1999]. Although important in an accurate kinematic description of folding over a listric thrust, the effects of both internal deformation and subtle geometric deviations from the idealized, circular fault plane are relatively minor and contribute <15% to the total uncertainties associated with our measurements. For simplicity, we neglect the potential effects of interseismic elastic strain storage during formation of a given strath in our displacement calculations [*Lavé and Avouac*, 2000; *Thompson et al.*, 2002].

[46] In areas where differential uplift of terrace treads occurs across a fault without significant differential tilting (e.g., Henburn, Figure 9e), we follow the same procedure described above for individual fault scarps for measuring slip (Figure 10a). Reported values may represent minimum estimates on the total displacement due to the potential for burial of older terrace surfaces in the aggrading footwall (Figure 8b). For all fault slip calculations, we use fault dip estimates from *Davis et al.* [2005] of 50 ± 18° (2σ), except for the North Central section near the Ohau River, where constraints from GPR suggest fault dips of 56 ± 9 ° (2σ) in the shallow subsurface. Conversion of measured fault displacements to slip rates is based on geochronologic data and regional climatic correlations that constrain the timing of surface formation throughout the Mackenzie basin. For both the Tekapo and Mount John terraces, we use reported exposure ages on equivalent moraines at Top McMillan Stream and nearby Lake Pukaki of 15.2 ± 2.4 ka (this study, Figure 5b) and 26.5 ± 4.0 ka [*Schaefer et al.*, 2001], respectively. Upper and lower bounds on the Balmoral outwash surface from OSL dates reported here (Tables 1a and 1b) and by *Amos et al.* [2007, Table 1b] suggest formation of this terrace between 72.4 ± 3.1 and 104.9 ± 6.3 ka (1σ). Despite complications surrounding the interpretation of reported CRN exposure dates for Wolds moraines and terraces, we utilize both the peak exposure age for dated strath capping gravels at Dry Stream of 110.8 ± 11.5 ka (Figure 5c) and the bounds on MIS 6 (130–191 ka) [*Lisiecki and Raymo*, 2005] as potential limits on the timing of Wolds surface formation. Slip rates calculated for Wolds surfaces use both age scenarios given the strong indication that the CRN dates at Dry Stream are likely biased toward younger ages. Younger Holocene surfaces are undated and excluded from the slip-rate calculations.

4.2. Subsurface Fault Geometry

[47] Application of the combined listric/planar thrust model to progressively tilted and differentially uplifted terrace segments along the Ostler fault zone also yields estimates of the fault geometry at depth from surveyed terrace profiles (Figures 7 and 9). Again, we follow *Amos et al.* [2007] in determining the depth of listric faulting and the orientation of the planar fault ramp adjoining the listric thrust segment in the deeper subsurface (Figure 10b). Both parameters depend on the measured width of backlimb tilting, the near-surface fault dip, and the position of the synclinal axial surface with respect to the fault's surface trace.

[48] An internal check on the calculated planar ramp dip comes from the observed magnitude of differential uplift across the fault for untilted terrace segments. There, the total vertical displacement should equal the product of fault slip calculated from backlimb tilting and the sine of the deeper ramp dip (Figure 10b). Although the actual geometry of the curved or listric fault arc is not perfectly circular, consistency among predicted and observed magnitudes of differential tilting and uplift for deformed terraces lends support to this model as a valid, first-order approximation of the fault geometry in the absence of subsurface seismic control [*Amos et al.*, 2007].

4.3. Uncertainties

[49] We use a Monte Carlo approach for estimating the uncertainty associated with calculated values of fault displacement, slip rate, and subsurface fault geometry. This technique has seen increasing use in neotectonic applications where the calculated parameter of interest (e.g., fault displacement or slip rate) depends on a large number of variables characterized by either continuous or discrete probability distribution functions (PDFs) [*Thompson et al.*, 2002; *Davis et al.*, 2005; *Amos et al.*, 2007] (Figure 10c). In each calculation, the Monte Carlo simulation samples PDFs associated with each input variable (e.g., surface age or fault dip) over twenty-five thousand trials to generate a histogram of the calculated parameter of interest (e.g., slip rate). Reported values for each output parameter reflect the mode and 95% confidence intervals of the resulting frequency distributions.

[50] We use a Gaussian PDF to characterize the uncertainties associated with regression parameters, fault dip, and surface ages constrained by CRN measurements on the Tekapo, Mount John, and Wolds terraces. For Balmoral terrace ages bracketed by OSL dating or correlation of the Wolds terrace with the marine isotopic record, we use a uniform, or boxcar uncertainty distribution for input into the Monte Carlo generator (Figure 10c). Displacement calculations from fault scarps also depend on an estimate of the fault position along the scarp face, because the actual fault planes are generally unexposed outside of trench exposures. As such, we use a trapezoidal distribution to describe the intersection position with the highest probabilities between one third and one half of the total scarp height from the base, diminishing to zero at the top and bottom of the scarp [*Thompson et al.*, 2002] (Figure 10c).

5. Results

5.1. Fault Displacement Profiles

[51] The total results of calculated fault displacements from scarp surveys and folded terrace profiles are compiled in Table S1 of the auxiliary material and Table 3, respectively.[1] For each individual fault section, plotting these measurements against along-strike distance from the southern fault termination allows construction of displacement profiles for the each of the four major surface age divisions (Figure 11). Individual profiles display a variety of shapes, and the positions of the maximum displacement for each section vary with

[1] Auxiliary materials are available in the HTML. doi:10.1029/2009TC002613.

Table 3. Measured Fault Displacements and Slip Rates from Folded Terrace Profiles

Profile Name[a]	Fault Section	Drainage	Scarp Location[b]			Along Strike Distance (km)[c]	Age Association[d]	Surface Age (ka)[e]	Slip (m)	95% Confidence Intervals		Slip Rate (mm/yr)	95% Confidence Intervals	
			Latitude	Longitude	Elevation (m)					(+)	(−)		(+)	(−)
T4E	Northern	Top McMillan Stream	−44.10406	170.04876	825.4	49.2	Tekapo	15.2 ± 2.4	22.5	12.2	2.9	1.6	1.1	0.4
T3W	Northern	Top McMillan Stream	−44.10431	170.04753	829.9	49.1	Mount John	26.5 ± 4.0	23.6	11.8	3.8	0.9	0.7	0.2
T4E	Haybarn	Top McMillan Stream	−44.10982	170.04931	772.6	48.6	Tekapo	15.2 ± 2.4	9.9	5.0	1.4	0.6	0.5	0.1
T2'S	Haybarn	Gladstone Stream	−44.14224	170.03814	701.6	44.9	Balmoral	73–105	56.4	30.8	6.3	0.7	0.4	0.1
T2S	Haybarn	Gladstone Stream	−44.14305	170.03757	700.9	44.8	Balmoral	73–105	91.0	50.3	10.2	1.1	0.6	0.3
T3N	Haybarn	Gladstone Stream	−44.13898	170.04016	701.8	45.2	Mount John	26.5 ± 4.0	24.4	11.7	3.6	0.9	0.7	0.2
T3S	Haybarn	Gladstone Stream	−44.14067	170.03890	702.9	45.0	Mount John	26.5 ± 4.0	22.1	10.9	3.2	0.8	0.6	0.2
T1S	Haybarn	Dry Stream	−44.17366	170.02579	536.0	41.2	Wolds	110.8 ± 11.5	210.8	109.1	34.1	1.8	1.3	0.4
T1 N (DEM)	Haybarn	Dry Stream	−44.16063	170.03445	545.0	42.8	Wolds	110.8 ± 11.5	196.4	99.1	32.4	1.7	1.1	0.3
T1S	Haybarn	Dry Stream	−44.17366	170.02579	536.0	41.2	Wolds MIS 6	130–191	210.8	109.1	34.1	1.3	0.8	0.3
T1 N (DEM)	Haybarn	Dry Stream	−44.16063	170.03445	545.0	42.8	Wolds MIS 6	130–191	196.4	99.1	32.4	1.2	0.8	0.2
T3S	Haybarn	Dry Stream	−44.16646	170.03204	613.6	42.1	Mount John	26.5 ± 4.0	16.2	9.5	2.1	0.6	0.5	0.2
T3'S	Haybarn	Dry Stream	−44.16917	170.02861	623.1	41.8	Mount John	26.5 ± 4.0	22.5	13.3	2.7	0.9	0.7	0.2
T2N	North Central	Ohau River	−44.24461	170.05413	511.9	34.2	Balmoral	73–105	65.5	9.5	5.0	0.7	0.2	0.1
T2N	North Central	Ohau River	−44.22689	170.05820	522.0	36.2	Balmoral	73–105	117.4	17.3	10.1	1.3	0.4	0.2
T3N	North Central	Ohau River	−44.25078	170.05155	514.0	33.4	Mount John	15.2 ± 2.4	22.2	3.2	1.8	1.4	0.8	0.3
T4N	North Central	Ohau River	−44.26960	170.04956	482.0	31.4	Tekapo	15.2 ± 2.4	29.8	4.4	2.4	1.8	1.1	0.3
T2 (DEM)	North Central	Clearburn	−44.36267	170.00306	506.0	20.4	Balmoral	73–105	131.4	68.8	17.8	1.5	0.9	0.3
T3 (DEM)	North Central	Clearburn	−44.34737	170.00280	527.0	22.0	Mount John	26.5 ± 4.0	49.2	25.3	7.8	1.8	1.4	0.5
T3′ (DEM)	North Central	Clearburn	−44.34508	170.00424	530.0	22.3	Mount John	26.5 ± 4.0	36.3	20.3	5.0	1.4	1.0	0.4
T1N western fold	South Central	Willowbank Saddle	−44.40081	169.97066	523.4	15.6	Wolds	110.8 ± 11.5	190.8	97.7	25.9	1.7	1.1	0.3
T1N frontal fold	North Central	Willowbank Saddle	−44.40461	169.98334	456.7	15.5	Wolds	110.8 ± 11.5	124.1	60.3	19.3	1.1	0.7	0.2
T1S western fold	South Central	Willowbank Saddle	−44.39925	169.97195	535.3	15.8	Wolds	110.8 ± 11.5	179.3	90.7	27.0	1.6	1.0	0.3
T1S frontal fold	North Central	Willowbank Saddle	−44.39902	169.97195	535.3	15.8	Wolds	110.8 ± 11.5	147.1	76.5	22.5	1.3	0.8	0.3
T1N western fold	South Central	Willowbank Saddle	−44.40081	169.97066	523.4	15.6	Wolds MIS 6	130–191	190.8	97.7	25.9	1.2	0.7	0.3
T1N frontal fold	North Central	Willowbank Saddle	−44.40461	169.98334	456.7	15.5	Wolds MIS 6	130–192	124.1	60.3	19.3	0.8	0.5	0.2
T1S western fold	South Central	Willowbank Saddle	−44.39925	169.97195	535.3	15.8	Wolds MIS 6	130–193	179.3	90.7	27.0	1.1	0.7	0.2
T1S frontal fold	North Central	Willowbank Saddle	−44.39902	169.97195	535.3	15.8	Wolds MIS 6	130–194	147.1	76.5	22.5	0.9	0.6	0.2
T1N total	Central	Willowbank Saddle	−44.40461	169.98334	456.7	15.5	Wolds	110.8 ± 11.5	322.2	87.9	39.7	2.8	1.1	0.4
T1S total	Central	Willowbank Saddle	−44.40438	169.97204	535.3	15.8	Wolds	110.8 ± 11.5	332.1	89.5	41.0	2.9	1.1	0.4
T1N total	Central	Willowbank Saddle	−44.40461	169.98334	456.7	15.5	Wolds MIS 6	130–191	322.2	87.9	39.7	2.0	0.7	0.4
T1S total	Central	Willowbank Saddle	−44.40438	169.97204	535.3	15.8	Wolds MIS 6	130–191	332.1	89.5	41.0	2.1	0.7	0.4

[a]Topographic profiles taken from the TOPSAR 10-m digital elevation model (DEM) are noted in parentheses.
[b]Coordinates represent intersection of survey profiles with the fault surface trace.
[c]Distance from the southern fault tip along a projection line fit to the average fault strike (015°).
[d]Age categorization based on the proposed Mackenzie Basin terrace stratigraphy. Ages for Wolds surfaces come from CRN surface clast ages at Dry Stream (this study). Tentative correlation of Wolds surfaces with MIS 6 reflects the probable older age of these surfaces.
[e]Ages for Tekapo surfaces from CRN moraine exposure ages (this study), while Mount John ages reflect reported CRN moraine exposure ages at Lake Pukaki by *Schaefer et al.* [2001]. Age ranges on MIS 6 from *Lisiecki and Raymo* [2005].

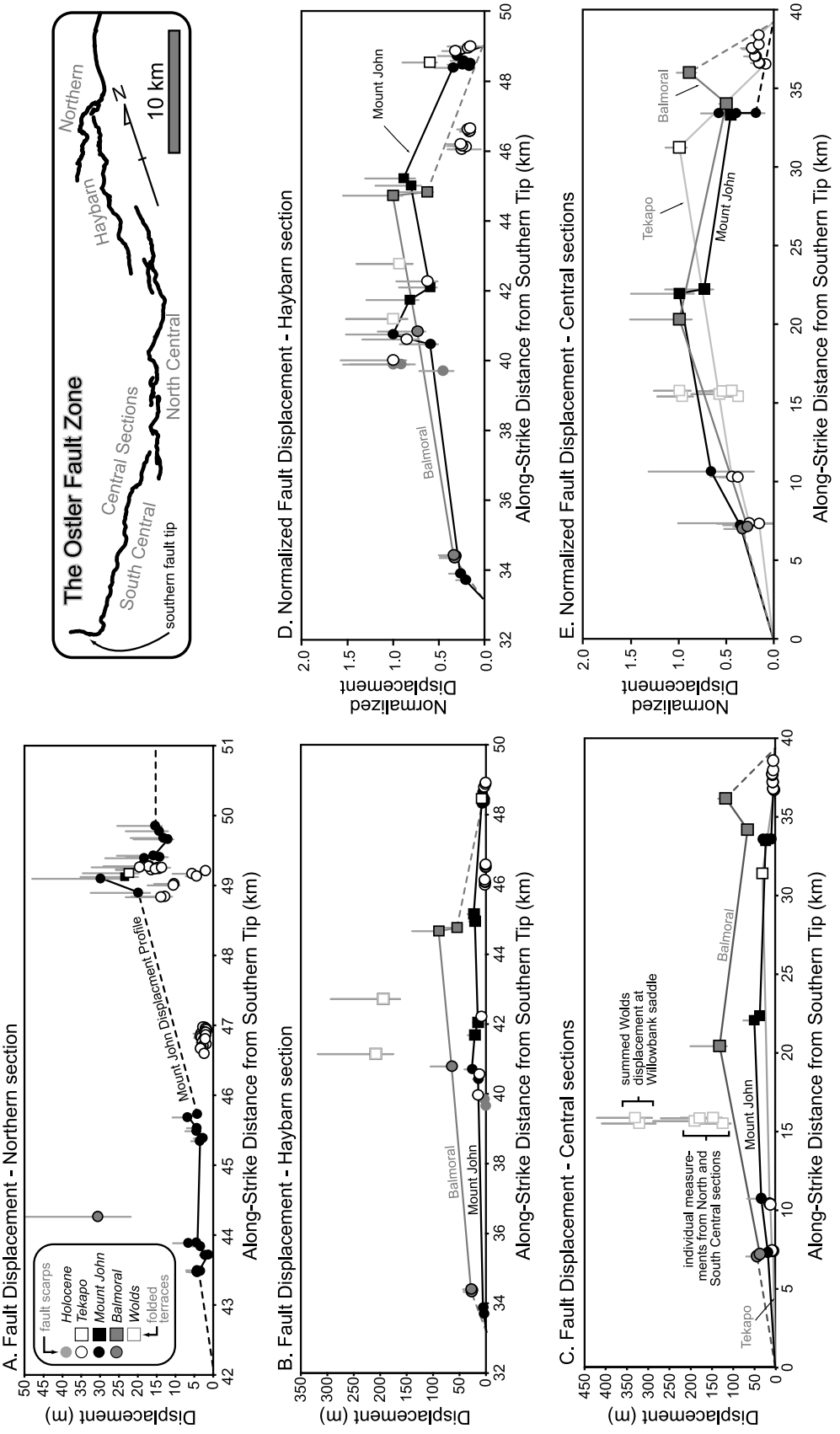
A. Fault Displacement - Northern section
Displacement (m)
Along-Strike Distance from Southern Tip (km)
fault scarps
Holocene
Tekapo
Mount John
Balmoral
Wolds
folded terraces
Mount John Displacement Profile
B. Fault Displacement - Haybarn section
Displacement (m)
Along-Strike Distance from Southern Tip (km)
Balmoral
Mount John
C. Fault Displacement - Central sections
Displacement (m)
Along-Strike Distance from Southern Tip (km)
summed Wolds displacement at Willowbank saddle
individual measurements from North and South Central sections
Balmoral
Mount John
Tekapo
The Ostler Fault Zone
Northern
Haybarn
Central Sections
South Central
North Central
southern fault tip
N
10 km
D. Normalized Fault Displacement - Haybarn section
Normalized Displacement
Along-Strike Distance from Southern Tip (km)
Mount John
Balmoral
E. Normalized Fault Displacement - Central sections
Normalized Displacement
Along-Strike Distance from Southern Tip (km)
Tekapo
Balmoral
Mount John

Figure 11

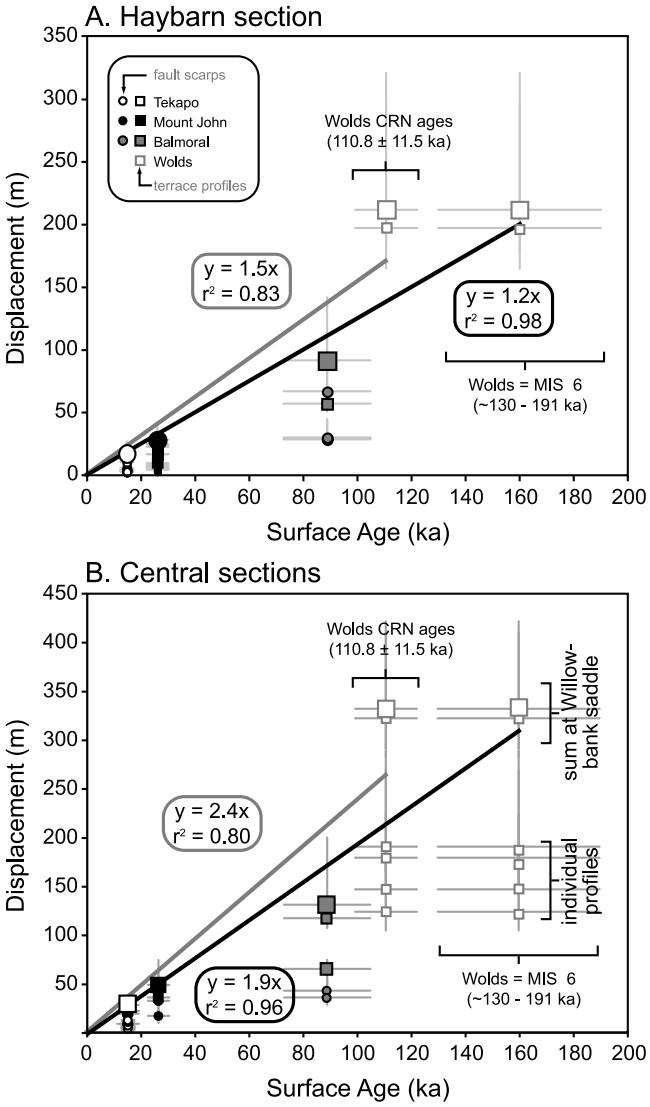

Figure 12. Calculated terrace displacements versus surface age along the (a) Haybarn and (b) Central Ostler fault zone sections. Linear regressions through the maximum displacements (large symbols) for each age division yield a measure of maximum slip rate for each fault strand based on either the peak CRN exposure age for the T1 terrace at Dry Stream or correlation of the Wolds surface with MIS 6. Slip rates for the Central section reflect summed displacements across the North Central and South Central faults at Willowbank saddle.

respect to the total distance along the fault trace. In contrast with the irregular, stepped profile observed for the Mount John surface on the Northern fault section (Figure 11a), the displacement profiles for the Haybarn and Central sections display roughly linear slip gradients tapering away from centralized displacement maxima to typically steeper gradients near the fault termini (Figures 11b and 11c). Similar slip distributions are observed for individual scarp segments on the Ostler fault [*Davis et al.*, 2005] and numerous other studied faults and fault zones [e.g., *Muraoka and Kamata*, 1983; *Peacock and Sanderson*, 1996; *Schlische et al.*, 1996; *Cowie and Roberts*, 2001; *Manighetti et al.*, 2001]. Additionally, slip maxima for the Mount John and Balmoral surface ages occur at roughly the same along-strike position for the Haybarn and Central sections (Figures 11b and 11c). The general lack of older deformed surfaces on the Northern fault strand precludes assessment of this relationship (Figure 11a). The degree of asymmetry observed in the displacement profiles varies among fault strands, a feature also evident in profiles measured along individual Ostler fault scarps [*Davis et al.*, 2005]. In addition to the strongly north-skewed profile for the Northern fault, central sections of the Ostler fault zone, as a whole, display a slight northern asymmetry, evidenced by steeper displacement gradients toward the northern fault tip (Figure 11c). Slip profiles for the Haybarn section are roughly symmetrical with a central displacement maximum (Figure 11b).

[52] The similarity among displacement profiles for multiple surface ages can be assessed by normalizing calculated values of fault slip by the maximum estimated displacement for each age division (Figures 11d and 11e) [*Nicol et al.*, 2005]. For the Haybarn and Central fault sections, normalized fault slip profiles are remarkably similar in shape (Figures 11d and 11e). Profiles for the North and South Central faults, when summed over the frontal and western folds, contribute to a broadly triangular to semi-elliptical shape for the total normalized Central section profile (Figure 11e). Such smoothly varying displacement profiles composed of multiple overlapping fault strands are characteristic of well-integrated, but segmented, fault zones or arrays [e.g., *Cartwright et al.*, 1995; *Dawers and Anders*, 1995].

[53] Taken as individual segments, slip profiles along the North and South Central strands are highly asymmetric with relatively steep displacement gradients near the overlap zone at Willowbank Saddle. The total, normalized slip distribution for the central Ostler fault, however, preserves only the modest northern asymmetry evident for individual surface age profiles (Figures 11c and 11e). The general symmetry about the center of the Haybarn displacement profile is also maintained through normalization, although elevated slip gradients near the fault tips become increasingly pronounced (Figures 11b and 11d). Despite the likelihood of local irregularities in the displacement profiles below the ~2–5 km resolution of our data set [*Davis et al.*, 2005; *Nicol et al.*, 2005], the general equivalence among the measured slip distributions for the Haybarn and Central sections is

Figure 11. Displacement profiles measured from fault scarp surveys and terrace profiles along the (a) Northern, (b) Haybarn, and (c) Central Ostler fault zone sections. Along-strike distance is measured from the southern fault tip near the Ahuriri River along a trend line of 015°. Normalized displacement profiles for the maximum slip within each age division are shown for the (d) Haybarn and (e) Central Ostler fault. Central Ostler fault zone profiles show the summed displacement across Willowbank saddle for individual slip measurements across the North and South Central fault sections.

consistent with maintenance of a similar displacement profile for fault growth since Balmoral time. A general lack of constraints on the tip positions of surfaces older than the Last Glacial Maximum, however, could potentially obscure the exact nature of the Balmoral displacement profile, which may have been affected by either erosion or aggradation during the Mount John or Tekapo intervals.

5.2. Fault Slip Rates

[54] When plotted against surface age, calculated fault displacements permit inspection of slip rates and slip rate variability for major sections of the Ostler fault zone (Figure 12). Apparent scatter in the total fault slip for each age division suggests along-strike variability [*Cowie and Roberts*, 2001], consistent with the observed displacement gradients along individual sections (Figure 11). Linear regressions through the maximum calculated fault displacements for each surface age are fixed through the origin and yield estimates of maximum fault slip rates for both the Haybarn and Central sections (Figures 12a and 12b, respectively). Regressions for each fault section represent different age scenarios for the Wolds terraces at Dry Stream (Figures 6a and 7c) and Willowbank Saddle (Figures 8a and 9c). Slip rates calculated for these surfaces utilize both the peak CRN exposure age calculated for the Dry Stream T1 terrace, which is likely minimum age, or a generalized correlation with MIS 6, bracketed between 130 and 191 ka [*Lisiecki and Raymo*, 2005].

[55] Maximum calculated slip rates for the Haybarn section vary between 1.5 and 1.2 mm/yr, based on a minimum CRN-exposure age for the Wolds surface or correlation with MIS 6, respectively (Figure 12a). The correlation coefficients for these linear regressions suggest a slightly better fit for the older, MIS 6 bracketing age. Similarly, using the summed Wolds displacement at Willowbank saddle for the North Central and South Central sections yields a good linear correlation between maximum fault slip and surface age (Figure 12b). For the Central sections, maximum fault slip rates vary between 2.4 and 1.9 mm/yr based on either a minimum CRN age for the Wolds surface or correlation with MIS 6, respectively. Given the likelihood that the CRN age is significantly younger than the actual age of the Wolds surface, our preferred estimate of maximum slip rates on the Haybarn and Central fault sections (1.2–1.9 mm/yr, respectively) utilizes this generalized climatic correlation. These slip-rate values are slightly higher but stand in general agreement with previously reported values for the Central fault section of 1.1–1.7 mm/yr based on kinematic modeling of the deformed Ohau River terraces [*Amos et al.*, 2007]. Good linear fits between maximum displacements and surface age (Figure 12) also indicate that the fastest slipping portions of each fault section were able to persist through time without the major variations in slip rate that are characteristic of some other active faults of comparable size over this timescale [*Villamor et al.*, 2007].

[56] Our fault slip-rate calculations from fault scarp profiles and folded terraces (Tables S1 and 3, respectively) represent the mode of frequency distributions from the Monte Carlo routine and associated 95% confidence intervals. With the exception of the Mount John terrace immediately north of the Ohau River (T3′, Figures 4b), fault slip rates for individual profiles reflect surface ages as discussed in previous sections. Very similar scarp heights of ~20 m on the Mount John and Tekapo surfaces (Figure 8a) suggest that the temporal gap between formation of these surfaces was shorter than the fault's recurrence interval [*Amos et al.*, 2007]. Use of a Tekapo age for this surface thus more appropriately reflects the time period since the terrace began recording deformation.

[57] Along-strike compilation of calculated slip rates (Figure 13) reveals a similar pattern to the normalized displacement profiles for each section of the Ostler fault zone (Figures 11d and 11e). Because displacement rates reflect normalization of measured fault slip by surface age, resemblance between the data sets is consistent with maintenance of constant displacement rate gradients since formation of the Wolds surface. In this context, the Northern displacement rate profile is irregular, with a pronounced increase in fault slip rates from <0.5 mm/yr to values between 0.5 and 1.0 mm/yr near the northern termination of the Haybarn fault (Figure 13a). The Northern slip-rate profile also has a number of local maxima and irregularities similar to those described by *Davis et al.* [2005] for displacement profiles along individual scarps. Slip-rate profiles for the Haybarn and Central fault sections exhibit comparable unevenness, although the general profile forms an approximately semi-elliptical shape (Figures 13b and 13c). Displacement rate maxima for these profiles are roughly centrally located with approximately linear slip-rate gradients tapering to zero at the fault tips. Gradients in displacement rate are generally highest in zones of section overlap, in agreement with observations from other segmented fault arrays [e.g., *Schlische et al.*, 1996; *Gupta and Scholz*, 2000; *Commins et al.*, 2005].

5.3. Fault Structure

[58] Fault geometry predicted from the listric model (Figure 10b) suggests systematic along-strike variability for major segments of the Ostler fault zone (Figure 14). The total results of calculated depths of listric and planar ramps dips (Table 4) reveal estimated ramp dips that range between 12° and 39°, with gentler dips predicted for northern half of the fault zone (Figure 14a). As discussed previously, the observed magnitude of differential uplift of untilted terraces over the planar ramp should be compatible with the sine of the calculated dip and the slip magnitude measured from backlimb tilting (Figure 10b and Table 3). Vertical offset of untilted Mount John surfaces of 3–6 m across the fault at Top McMillan and Gladstone Streams (Figures 6a and 7) matches differential uplift predicted using the ~20–25 m of calculated fault slip and estimated ramp dips of 12–18° (Tables 3 and 4). Similarly, differential uplift of Mount John surfaces at the Ohau River (~10 m) and Clearburn (~30 m) (Figure 9), agrees well with estimated ramp dips of 12° and 35°, respectively, and fault slips of 30–50 m as measured from tilted fold backlimbs (Table 3). Correspondence between observed and predicted differential uplift magnitudes lends support to the listric model as a valid approximation of faulting in these locations. At Dry Stream, we

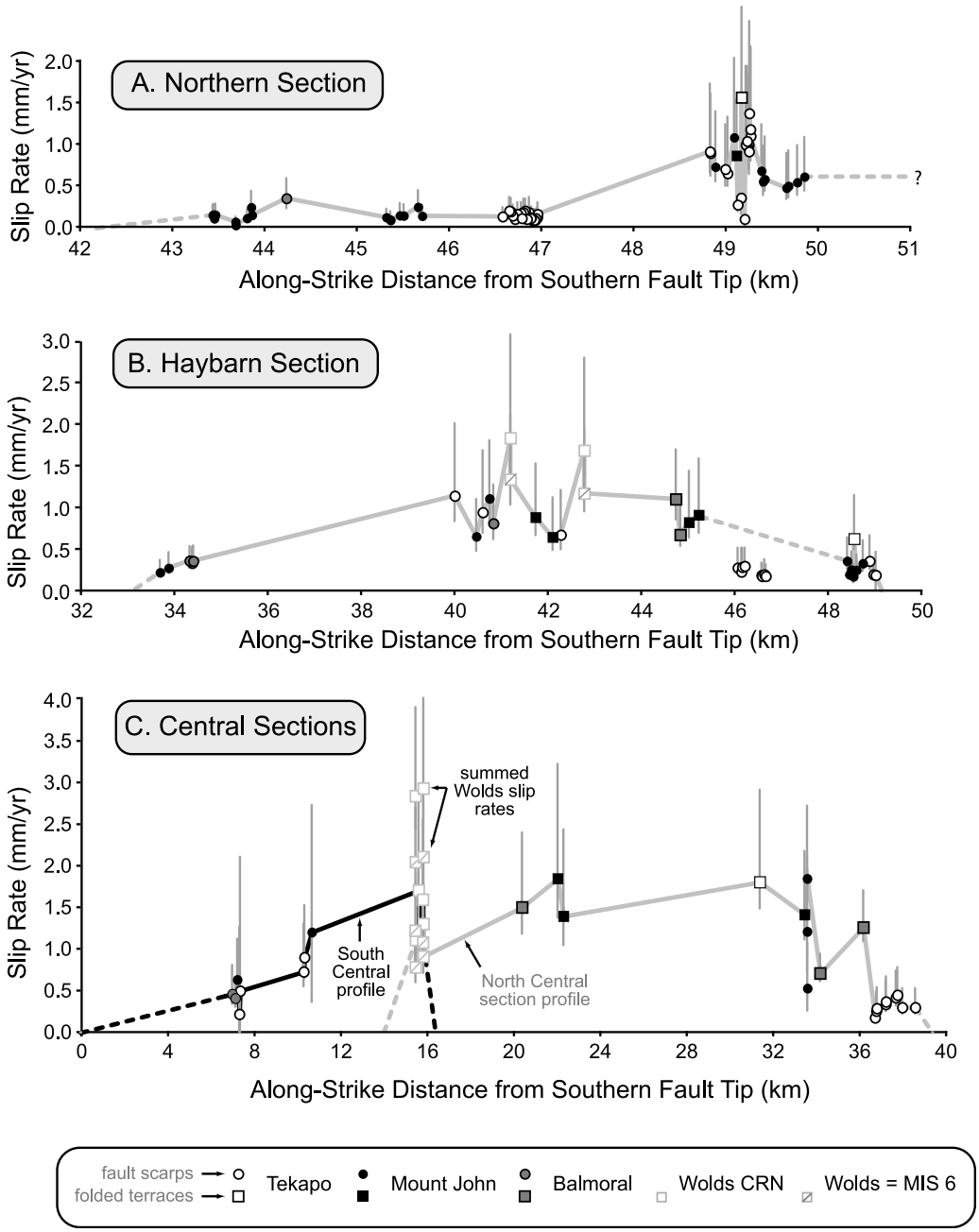

Figure 13. Slip rate profiles for the (a) Northern, (b) Haybarn, and (c) Central sections of the Ostler fault zone. Along-strike distance is measured from the southern fault tip along a projection line oriented 015°. Profiles for the Central section reflect both individual measurements for the North and South Central faults, as well as the summed slip rate at Willowbank saddle.

use the T1 Wolds surface as a reference for fault geometry calculations given the potential for relatively small tilts (0.4–0.6°) to affect the measurement of the backlimb width on the deformed Mount John terrace (Figure 7c) [*Amos et al.*, 2007]. A lack of corresponding surfaces in the footwall at both Gladstone Stream and Willowbank Saddle prevents evaluation of predicted ramp dip values because aggradation has obscured the net vertical offset of terraces across the fault.

[59] The transition depth between listric faulting and the planar ramp also varies for each major section of the Ostler fault zone (Figure 14b). For the Northern, Haybarn, and North Central fault sections, ramp depth defines an approximately bow-shaped profile along-strike, with maximum depths of 0.7–0.8 km between Dry Stream and the Ohau River. Farther south, the depth of listric faulting decreases to 0.3 km, before jumping to predicted values of

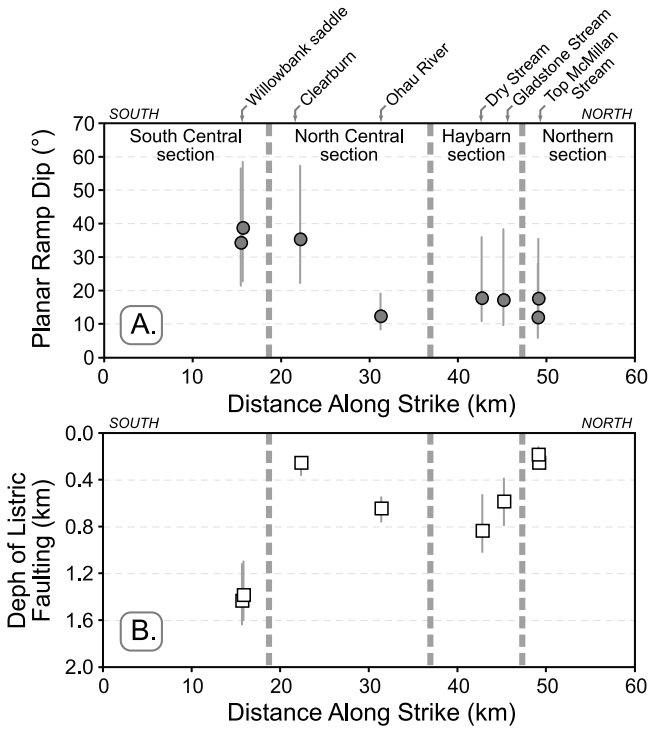

Figure 14. Along-strike predictions of fault geometry output from the listric fault model. (a) Estimated dips of the planar ramp adjoining the listric fault in the deeper subsurface. Ramp dips display a systematic southward deepening across major fault sections. (b) Transition depth between listric and planar faulting. Note the prominent jump to deeper planar ramps between the North and South Central fault sections at Willowbank saddle.

1.4 km after crossing the transfer zone to the South Central section at Willowbank Saddle (Figure 14b).

[60] An independent check on the geometric predictions of the listric fault model comes from seismic reflection and refraction profiles collected across the Clearburn and Willowbank saddle paleo-outwash valleys [*Ghisetti et al.*, 2007; *Campbell et al.*, 2010] (Figure 1). In each location, seismic profiles are interpreted to show relatively constant fault dips of 45–60°W reaching depths between ~1–1.5 km. The Ostler fault penetrates Torlesse greywacke basement in each profile and offsets several packages of Plio-Pleistocene sediments. Each seismic line also contains numerous fault strands and splays that do not offset the ground surface, some with substantially gentler dips approaching ~25–35° [*Campbell et al.*, 2010]. Overall, these results match our prediction of comparatively minor listric fault curvature at Clearburn and Willowbank saddle based on the wavelength of backlimb tilting (Figure 14 and Table 4). At Clearburn, the predicted fault geometry from folded Mount John and Balmoral surfaces suggests that the listric segment of the fault is confined to within the ~300 m of the surface. Below this depth, the fault intersects a planar fault ramp dipping at 35 +22/−13° at 95% confidence (Table 4). The relatively short arc of the listric fault segment and the small change in surface fault dip (50 ± 18°, 2σ) at Clearburn are supported by the comparatively short wavelength (~0.5 km) of backlimb tilting observed in the terrace profiles at this location (Figure 9b and Table 4). Additionally, the relatively high ratio of total differential uplift of the Mount John surface compared to the total slip calculated from the listric fault model supports a relatively steep fault plane at depth. This predicted geometry appears compatible with uninterpreted seismic profiles presented in both *Ghisetti et al.* [2007] and *Campbell et al.* [2010].

[61] Similarly, the fault geometry predicted from folded terraces at Willowbank saddle includes relatively modest fault curvature corresponding to a transition in surface fault dip (50 ± 18°, 2σ) to a planar fault ramp dipping between 34 +22/−13° and 39 +20/−16° (Figure 14 and Table 4). This transition in dip occurs at ~1.4 km depth at Willowbank saddle, consistent with the relatively broad wavelength (~3 km, Table 4) of fold backlimbs and the comparatively high ratio of total vertical throw to fault slip on the T1 Wolds surface (Figure 9c). This result also matches well the range of fault dips between ~45–60° interpreted from

Table 4. Predictions of Subsurface Fault Geometry

Profile Name[a]	Drainage	Fault Segment	Along Strike Distance[b] (km)	Backlimb Width[c] (km)	Synclinal Axial Surface Distance[d] (km)	Surface Fault Dip	Planar Ramp Dip θ_2	95% Confidence Intervals (+)	95% Confidence Intervals (−)	Ramp Depth[e] (km)	95% Confidence Intervals (+)	95% Confidence Intervals (−)
T3E	Top McMillan Stream	Northern	49.2	0.63	0.45	50 ± 18°	18	18	7	0.3	0.0	0.1
T3W	Top McMillan Stream	Northern	49.1	0.42	0.34	50 ± 18°	12	16	6	0.2	0.1	0.1
T3N	Gladstone Stream	Haybarn	45.2	1.55	1.09	50 ± 18°	17	21	8	0.6	0.2	0.2
T1N (DEM)	Dry Stream	Haybarn	42.8	*2.02*	1.45	50 ± 18°	18	18	7	0.8	0.2	0.3
T4N (DEM)	Ohau River	North Central	31.4	1.30	1.11	56 ± 9°	12	7	4	0.7	0.1	0.1
T3′ (DEM)	Clearburn	North Central	22.3	1.57	0.56	50 ± 18°	35	22	13	0.3	0.1	0.0
T1N western fold	Willowbank Saddle	South Central	15.6	*7.12*	2.74	50 ± 18°	34	22	13	1.4	0.2	0.3
T1S western fold	Willowbank Saddle	South Central	15.8	*7.82*	2.71	50 ± 18°	39	20	16	1.4	0.2	0.3

[a]Terrace profiles used to calculate fault geometry from the listric fault model. Profiles taken from the TOPSAR 10-m digital elevation model (DEM) are noted in parentheses.

[b]Measured distance from the southern fault termination along a projection line fit to the average fault strike (015°).

[c]Backlimb width is measured from survey profiles by projecting the tilted backlimb regression line to the average elevation of the untilted footwall surface. Italics indicate profiled surfaces that do not correlate across the fault trace. See *Amos et al.* [2007].

[d]Measured distance between the fault trace and the synclinal axial surface position.

[e]Fault dips in the shallow subsurface from *Davis et al.* [2005] and *Amos et al.* [2007]. Uncertainties represent 2 s errors on measured fault dips.

seismic reflection data at Willowbank Saddle [*Ghisetti et al.*, 2007] and confirms the listric fault model as a good first-order approximation of subsurface fault geometry.

[62] In our previous study, we note a general correspondence between basin depth and the depth of listric faulting both where the Ostler fault intersects the Ohau River and for the Irishman Creek fault to the northeast [*Amos et al.*, 2007]. The proximity of the Northern and Haybarn fault sections to the foot of the Ben Ohau Range (Figure 1) does imply a decrease in basin depth north of the Ohau River in concert with a systematic decrease in the depth of listric faulting (Figure 14b). The area immediately east of the Ben Ohau Range also coincides with relatively gentle ramp dips calculated for the deeper subsurface in comparison with Clearburn and Willowbank saddle (Figure 14a), where significant thickness of Plio-Pleistocene strata are exposed. Strath exposures along the Northern and Haybarn fault sections, however, suggest that listric faulting is neither restricted to nor ubiquitous within the region where Tertiary strata occur in the hanging wall. For example, folded terrace geometries at Top McMillan Stream suggest deformation over a curved fault plane (Figure 7a), despite the strict presence of Torlesse basement rocks in the uplifted hanging wall. Additionally, surface deformation patterns observed in the Henburn drainage, where exposed Tertiary rocks imply significant thicknesses of Cenozoic fill, are incompatible with deformation over a listric fault (Figure 9e). Similar deformation patterns also occur for the Fraser Stream terraces (Figure 7d), which represent straths cut directly into Torlesse bedrock. As such, systematic variation in fault geometry observed for the Ostler fault zone (Figure 14) reflects additional factors other than subsurface rock type. Correspondence between abrupt changes in ramp depth and major section boundaries, however, does indicate that predicted geometric variations do reflect actual differences in the deeper fault zone structure.

6. Discussion

6.1. Sources of Uncertainty in the Data Set

[63] The legitimacy of calculated fault displacements, slip rates, and geometric predictions strongly depends on the applicability of the listric thrust model (Figure 10b) in approximating the kinematics and geometry of deformation. Both hanging wall internal deformation and subtle variations in fault plane curvature undoubtedly influence our measurements. The cumulative effects these factors, however, are likely to introduce <15% of additional uncertainty for estimated fault displacements and displacement rates [*Amos et al.*, 2007]. Deviations from the idealized, circular listric fault that are manifest in the terrace profiles as localized convexities or concavities along the folded backlimb may result from a modest increase or reduction, respectively, of the radius of fault- plane curvature. Such departures from strictly planar backlimbs are indeed visible along the titled T2, Balmoral terraces preserved along the flanks of Gladstone Stream and the Ohau River (Figures 7b and 9a).

[64] Additionally, subsidiary thrusts evident along terrace profiles over Willowbank Saddle (Figure 9c) occur as localized flexural slip faults and typify internal deformation within the hanging wall prescribed by rigid rotation in the listric fault model [*Amos et al.*, 2007]. Observed terrace offsets of <5 m on these faults, however, suggests displacements of less than a few percent of the calculated ~180 m of slip represented by the folded Wolds terrace. Thus, although important in allowing the hanging wall to adjust to fault plane curvature, slip along such structures does not violate the geometric predictions of the rigid rotation model [*Seeber and Sorlien*, 2000] or detract significantly from the accuracy of our predictions.

[65] Contributions to the total uncertainty in calculated fault displacement, slip rate, and fault geometry are dominated by uncertainty in shallow subsurface fault dip. Observed spatial variability in this parameter from GPR measurements [*McClymont et al.*, 2008] indicates a range in fault dips compatible with the relatively broad normal distribution $50 \pm 18°$ (2σ) used in the Monte Carlo simulation. Relatively gentle fault dips at the end of this spectrum contribute to the broad tails and higher upper bounds of output histograms for fault displacement and slip-rate (Figure 10c).

[66] Errors resulting from projecting terrace profiles oblique to axial surface traces may also contribute to uncertainties that are unaccounted for in the Monte Carlo simulation. Although the magnitude of this effect depends on the radius of fault curvature and the degree of backlimb tilting, a 0.1° error along the measured backlimb corresponds to <10% error in calculated fault displacement at tilts greater than 1° for the Ostler fault zone. Other sources of error may stem from approximating the initial, undeformed geometry of terrace surfaces using modern long profiles or linear fits to surveyed stream reaches (see discussion above). The effects of these uncertainties are potentially most pronounced for subtle tilts on younger Tekapo and Mount John surfaces. Such uncertainties would also affect areas where rivers make relatively large bends with respect to our projection lines (e.g., Fraser Stream, Figure 6a) or places where a formerly larger river (that created the terraces) has been replaced by a much smaller, lower discharge channel (e.g., Clearburn, Figure 8a). Nevertheless, several lines of evidence point to the overall robustness of our results, such as (1) good correspondence of calculated slip rates (Tables S1 and 3) with previous estimates for portions of the Ostler fault zone [*Blick et al.*, 1989; *Read and Blick*, 1991; *Davis et al.*, 2005; *Amos et al.*, 2007], (2) similarities between measured displacement profiles (Figures 11 and 13) and those reported for other faults [e.g., *Manighetti et al.*, 2001], and (3) the presence of internal and independent checks on predicted fault geometries.

6.2. Fault Linkage and Segment Interaction

[67] Measured along-strike displacement and slip-rate profiles for major sections of the Ostler fault zone imply a significant degree of interaction and displacement transfer among individual fault strands (Figures 11 and 13). Section interaction and fault linkage has long been recognized as an important process for fault growth [e.g., *Peacock and Sanderson*, 1991] and is typically evident through (1) observations of complementary asymmetry of displacement

profiles among overlapping fault segments [*Schlische et al.*, 1996; *Gupta and Scholz*, 2000], or (2) contributions of individual segments to a cumulative displacement profile resembling that of an individual fault [*Cartwright et al.*, 1995; *Dawers and Anders*, 1995; *Commins et al.*, 2005]. For the Ostler fault zone, evaluation of displacement profiles for individual scarps and for the fault zone as a whole reveals evidence for segment interaction at a variety of spatial scales. Measured displacement and slip rate profiles along the Northern fault section near Top McMillan Stream exemplify this interconnection (Figure 15). There, a total of 23 fault scarp surveys along a prominent right step-over reveal complementary displacements and slip-rate gradients across the zone of overlap. Similar observations for overlapping displacement profiles were reported by *Davis et al.* [2005] at the scale of individual scarps for both the Haybarn and North Central fault sections. At Top McMillan Stream, the total displacement profile summed over each strand also exhibits a distinct minima in the transfer zone (Figures 15c and 15d), interpreted for other sections by *Davis et al.* [2005] as representing incomplete or incipient fault linkage [*Dawers et al.*, 1993].

[68] As discussed in previous sections, compilation of along-strike displacement and slip rate measurements also reveals complementary asymmetry in profiles for the North and South Central fault sections (Figures 11 and 13). Despite being composed of multiple overlapping splays and strands (Figure 6b and 8), the total normalized slip summed across each section reveals a relatively smoothly varying displacement profile for the central Ostler fault (Figure 11c). Displacement and slip rate gradients are again highest in the zone of overlap at Willowbank saddle (Figure 13c), suggestive of interaction among these adjacent strands as slip accumulates [*Schlische et al.*, 1996; *Gupta and Scholz*, 2000; *Kim and Sanderson*, 2005]. Soft linkage of these sections will most likely persist until breaching of the relay ramp at Willowbank saddle enables formation of a thoroughgoing Central fault section to produce an overall smooth displacement profile.

[69] Evidence for fault interaction and displacement transfer is especially pronounced at the scale of major sections constituting the entire Ostler fault zone. Superimposing displacement rate profiles for the Northern, Haybarn, and Central strands (Figure 16) reveals a composite displacement profile characterized by a gradual increase in slip rate from the south toward a maximum of ~2 mm/yr along the Central section, eventually tapering to values between 0.5 and 1.0 mm/yr to the north. Continuation of the Northern section as a bedrock scarp into the Ben Ohau Range (Figure 1) precludes assessment of the total composite profile shape, although the overall morphology defined by our measurements is generally symmetric with only a slight skew toward higher rates in the south (Figure 16). Slip-rate gradients south of the central maximum display a relatively smooth and constant taper (Figures 13c and 16), reminiscent of the roughly linear gradients reported for other fault arrays [*Walsh and Watterson*, 1988; *Peacock and Sanderson*, 1996; *Cowie and Shipton*, 1998; *Manighetti et al.*, 2001; *Davis et al.*, 2005; *Nicol et al.*, 2005]. This morphology contrasts with the abrupt steepening of displacement gradients and profile shapes toward the fault tips within overlap zones on the Central and Haybarn faults (Figures 13c and 16). Self-similarity among the normalized slip distributions for these fault sections (Figures 11d and 11e) suggests that relatively steep displacement gradients are long-lived and have persisted near the fault tips since formation of the Balmoral surface. Maintenance of increased slip gradients in these locations may imply the presence of a barrier to fault propagation that restricts lengthening near the fault tip [*Nicol et al.*, 1996]. Such barriers result from changes in subsurface material properties or from local stress perturbations due to interactions between overlapping fault segments [*Nicol et al.*, 1996; *Manighetti et al.*, 2001; *Davis et al.*, 2005].

6.3. Implications for Lateral Growth of the Ostler Fault Zone

[70] Quantification of fault growth through lateral propagation requires along-strike temporal control on either deformed sedimentary strata [e.g., *Chen et al.*, 2007] or displaced geomorphic features [e.g., *Bennett et al.*, 2006]. Combined with sufficient age constraints, the evolution of displacement profiles often provide clues as to the relative importance of lengthening during fault growth. If growth occurs through the addition of coseismic slip during characteristic earthquakes with constant rupture length [*Schwartz and Coppersmith*, 1984], individual profile terminations for each time horizon will converge toward the fault tips in the total displacement profile (Figure 17a) [*Nicol et al.*, 2005]. For this scenario, the accumulated displacement profile gradually amplifies vertically, and the fault tips remain spatially pinned. In contrast, ruptures that progressively lengthen or propagate laterally will cause the profile tips for each successive time horizon to extend to increasing distances away from the location of maximum slip in the total displacement profile (Figure 17b) [*Childs et al.*, 2003; *Nicol et al.*, 2005]. Crucial to either interpretation are data of a sufficient resolution to reconstruct the tip locations for various age displacement profiles. Because of the tendency for younger terrace cutting or aggradation events to erode or obscure older surfaces, determining the dominant scenario for surface-rupturing faults is often challenging. Along the Ostler fault, however, we have sufficient data of different ages to be able to place limits on the magnitude of tip propagation through time.

[71] Displacement profiles for the Haybarn and Central sections of the Ostler fault zone (Figures 11b and 11c) imply that along-strike growth occurs through gradual amplification of a temporally persistent distribution of fault slip. Similarity among the normalized displacement profiles for each surface age division (Figures 11d and 11e) and the apparent maintenance of elevated slip rate gradients in transfer zones both point to preservation of a comparable slip distribution since Balmoral time (~70–100 ka). Surfaces preserved at the tips of these sections are of Mount John age or younger, however, and the exact position of the profile tips defined by the Balmoral surface cannot be exactly located. As such, any deformation recorded by Balmoral terraces that may have been present beyond their current locations remains unaccounted for in our study.

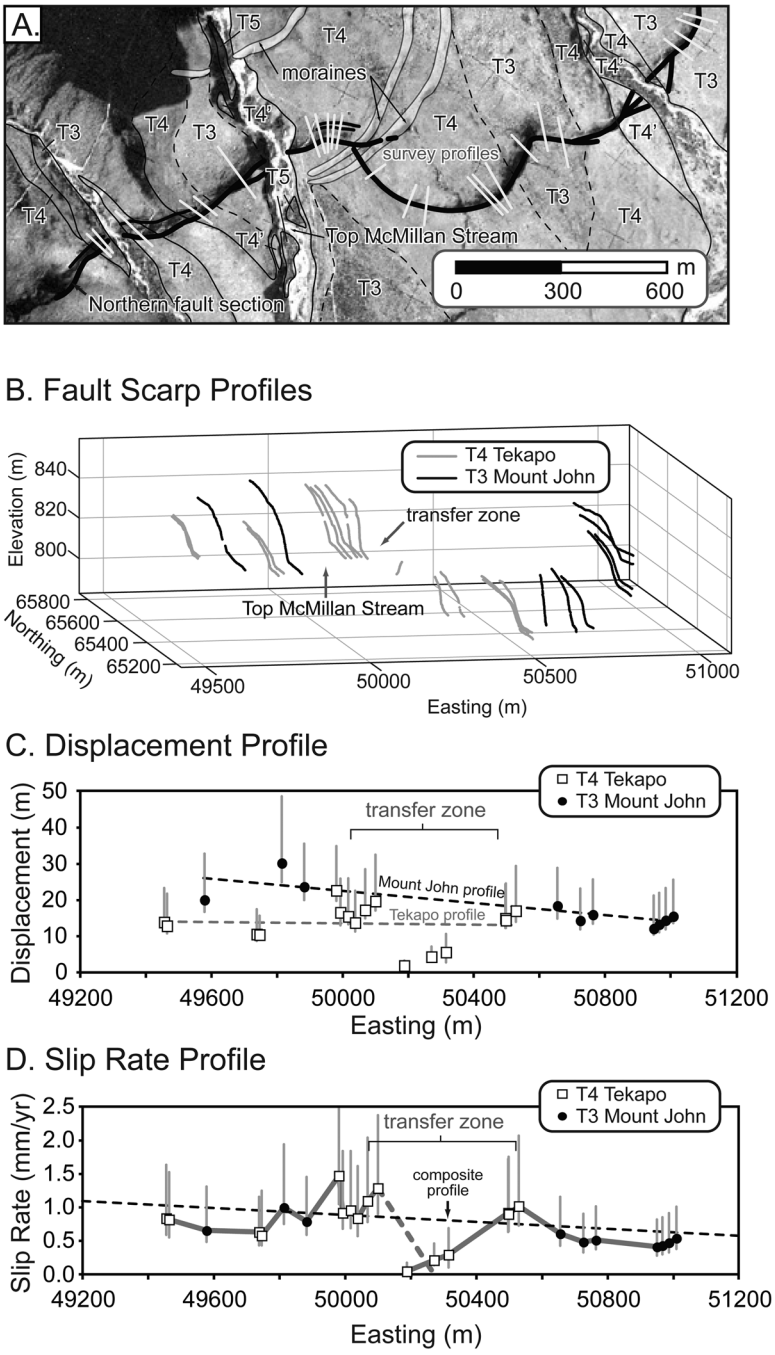

Figure 15. Displacement transfer at Top McMillan Stream. (a) Location map showing fault scarps, Tekapo and Mount John treads, moraines, and the approximate positions of fault scarp surveys. (b) Perspective image of survey data collected for fault scarps across the prominent transfer zone. (c and d) Displacement and slip rate profiles, respectively, measured from profiled fault scarps. Note the overall linear gradient in displacement and slip rate to the east and the overall displacement minima for the summed, composite profile across the transfer zone.

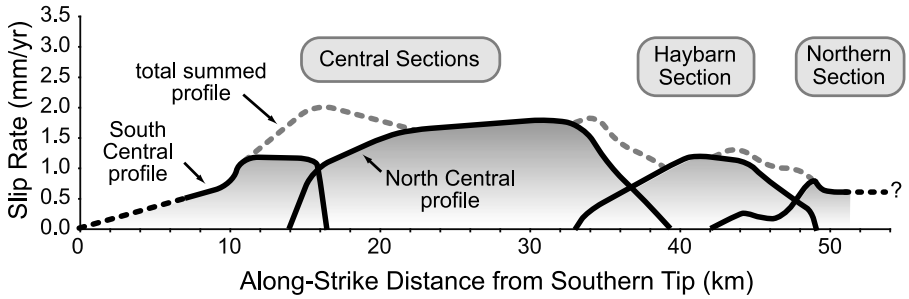

Figure 16. Composite slip-rate profile for the Ostler fault zone. Summing displacement rates over zones of segment overlap reveals a relatively broad, symmetric profile with smoothly varying displacement gradients outside of zones of fault overlap.

[72] Reported relationships between maximum displacement and segment length for the Ostler fault zone shed some light on potential incremental changes in fault length since creation of the Balmoral surface. In their study of individual scarps along the fault, *Davis et al.* [2005] found that maximum slip scales linearly as ~1% of surface trace length. Additionally, conversion of the maximum topographic relief along the central Ostler fault zone (~440 m, Figure 18a) to fault displacement (~575 m, using a 50° fault dip), suggests a similar scaling of ~1.5% of the total ~40 km section length [*Davis et al.*, 2005]. Calculated values of fault slip at Clearburn and the Ohau River indicate ~95 m of accumulated displacement between the Balmoral and Mount John surfaces at each location (Table 3), corresponding to a change in fault length of ~8 km using these scaling laws. If the position of maximum displacement has remained roughly constant over this interval, as suggested by our measurements (Figure 11), self-similar scaling of the total topographic envelope predicts the former fault tip positions between ~70–105 ka (Figure 18a). Exposures of deformed and differentially titled Late Quaternary and Tertiary strata near Fraser Stream (Figure 18b) [*Read*, 1984; *Amos et al.*, 2007] and south of Henburn (Figure 8) attest to an even longer history of deformation in these locations. This record

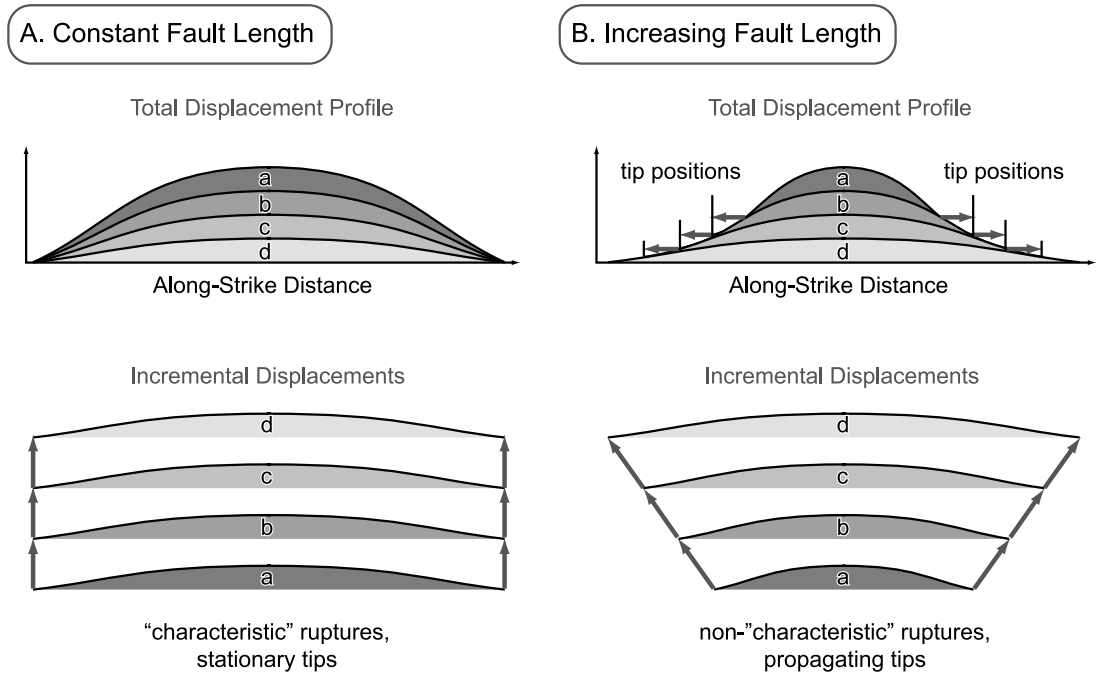

Figure 17. Hypothetical along-strike displacement profiles for fault growth (a) at a constant length and (b) through lateral tip propagation. Summing the incremental displacement profiles for ruptures a–d results in a broadly bell-shaped or semi-elliptical total slip distribution for each scenario. If "characteristic" ruptures occur at a constant fault length [*Schwartz and Coppersmith*, 1984], the total displacement profile will exhibit stationary fault tips for each age increment (Figure 17a). "Noncharacteristic" ruptures that increase in length with time will result in displacement profiles for each age increment that merge at progressively increasing distances away from the fault center (Figure 17b).

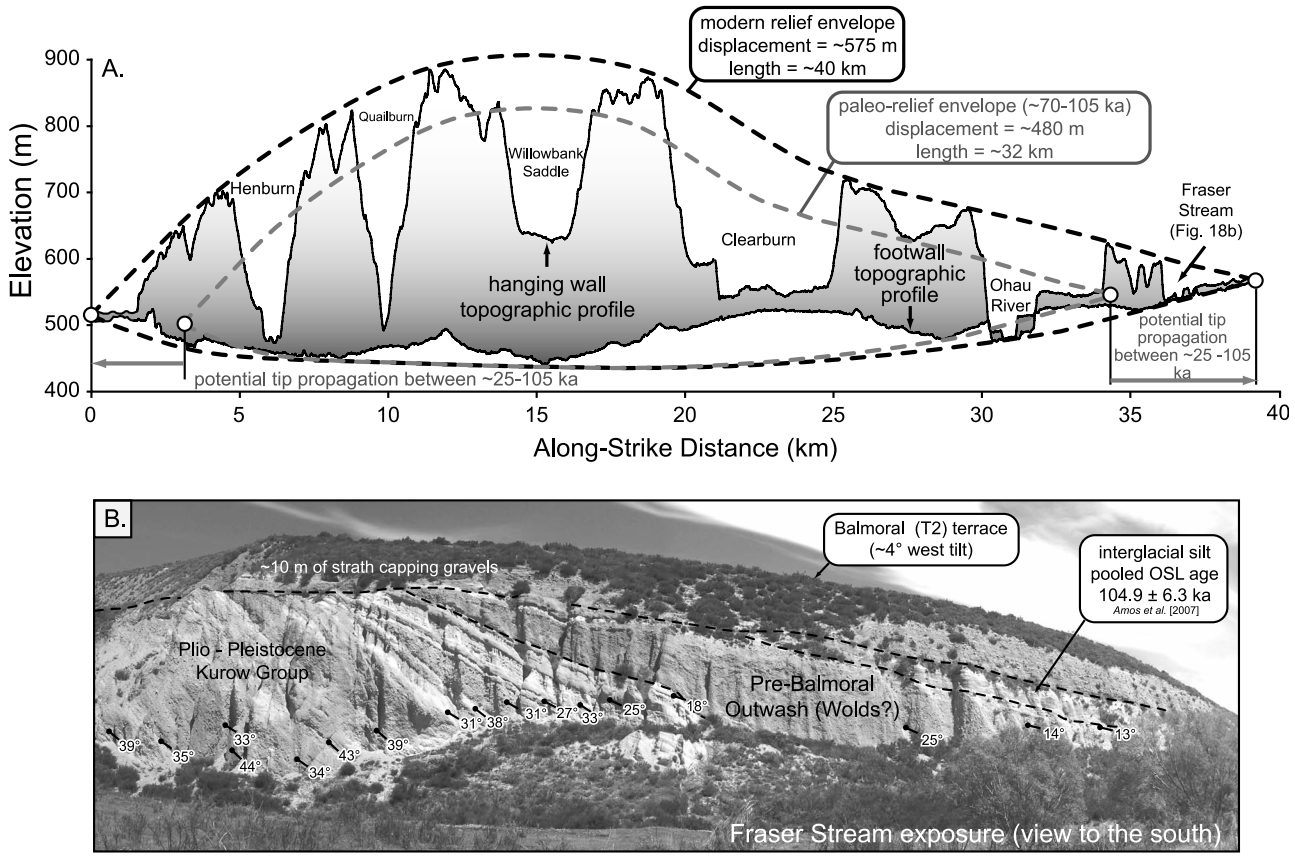

Figure 18. (a) Self-similar scaling of the total relief envelope for the central Ostler fault zone (as a proxy for displacement) predicts the paleo-tip locations and the amount of potential lateral propagation between formation of the Balmoral and Mount John surfaces. Removal of ~95 m of fault slip during this time period corresponds to a reduction in fault length of ~8 km. See text for discussion. Modified after *Davis et al.* [2005]. (b) Exposures of differentially tilted Plio-Pleistocene strata in a prominent angular unconformity at Fraser Stream suggest the relative longevity of deformation in this location prior to formation of the Balmoral strath. OSL dates from interglacial silts below the Balmoral capping gravels provide a maximum age on this outwash surface.

of deformation, moreover, contradicts the predicted position of the northern fault tip at Balmoral time, as inferred when fault growth is predicated using displacement–length scaling (Figure 18a). At Fraser Stream, folding and westward tilting of Plio-Pleistocene strata [*Mildenhall*, 2001] up to 45°W reflects either an earlier period of deformation unrelated to the modern Ostler fault, or the continued presence of fault-related folding for some significant duration (Figure 18b). The degree of westward tilting progressively decreases upward through the section, mimicking the modest tilt of the capping Balmoral terrace gravels (Figure 18b) and potentially supporting the latter scenario. These growth strata at Fraser Stream, including the wedge-shaped, pre-Balmoral conglomerate of probable Wolds age, clearly argue both for persistent differential hanging wall uplift and for the presence of rivers sufficiently powerful to successfully bevel off any uplifted Pleistocene strata until the end of Balmoral deposition. The Ohau River has subsequently incised up to ~125 m below the Balmoral surface (Figures 9a and 18a). Hence, we can conclude confidently that fault growth, at least for the northern tip of the Central section, occurred without significant fault lengthening over the past ~100 k.y. This result contradicts the predictions of length-displacement models (Figure 18a) and instead supports the fault growth model postulated by *Walsh et al.* [2002] in which slip accumulation occurs over a constant fault length after an initial period of rapid propagation.

[73] The northward younging of paleo-outwash valleys along the North Central section from Willowburn Saddle to Clearburn and then to the Ohau River (Figures 6b and 8) thus reflects factors other than simple fault lengthening. Despite satisfying the geomorphic criteria for lateral fold propagation [*Keller et al.*, 1999], the decreasing age and height of these wind gaps to the north instead represents lateral tilting in this direction due to sustained vertical amplification of the displacement profile. Away from the fault tips, gradients in the displacement profile are subtle and result in only a ~5–10 m difference in maximum slip on the

LGM surfaces at Clearburn and the Ohau River (Figure 11c). Nevertheless, calculated rates of drainage diversion from these wind gaps are rapid, exceeding 10 cm/yr based on various age scenarios for the Wolds surface. Although documented rates of lateral fold propagation from deformed geomorphic surfaces range up to several millimeters or centimeters per year [*Keller et al.*, 1998; *Jackson et al.*, 2002; *Bennett et al.*, 2005; *Chen et al.*, 2007], drainage deflection rates along the Ostler fault zone are not directly related to the kinematics of lengthwise thrust growth.

[74] Geomorphologic factors also contribute to the observed pattern of northward drainage diversion. First, the observed continuity of Mount John surfaces between the Clearburn outwash valley and the Ohau River implies that glacial outwash was able to occupy more than one water gap at a given time. For a relatively broad glacial terminus, such as that of the Ohau paleoglacier, the presence of two, widely separated outwash channels would not be unexpected. Once the glacier retreated, however, a single river channel would have formed across the terminal moraine complex. Given the pulsed nature of both terrace formation and glacial outwash, steady accumulation of slip during prolonged channel downcutting during interglacial periods would tend to funnel future drainage into the less deformed of the two valleys. Subsequent fluvial incision into these surfaces, driven by climatically controlled variations in discharge and sediment flux, also controls future patterns of outwash deposition by promoting drainage entrenchment. Such a scenario explains confinement of Tekapo outwash surfaces within the Ohau River Valley, despite a hiatus in deformation in this location since Mount John time.

[75] The question remains as to why growth of the Ostler fault zone occurred at a fixed length during the Late Quaternary. Displacement accumulation at near-constant fault lengths has been documented for other fault zones similar in scale to the Ostler fault, attributable to either (1) reactivation of pre-existing or inherited structures from previous periods of deformation [*Meyer et al.*, 2002; *Nicol et al.*, 2005], or (2) barriers to fault propagation due to mechanical interaction among individual faults within a relatively mature or established fault array [*Morewood and Roberts*, 1999; *Poulimenos*, 2000; *Childs et al.*, 2003]. In the central South Island of New Zealand, present-day patterns of deformation clearly reflect the influence of pre-existing structure and crustal composition [*Upton et al.*, 2009]. Reactivation of formerly extensional faults as active thrusts has been documented in Otago [e.g., *Litchfield*, 2001] and elsewhere in the South Island [*Ghisetti and Sibson*, 2006]. As such, the suggestion that the Mackenzie Basin may be undergoing compressional inversion controlled by reverse slip on Ostler fault [*Ghisetti et al.*, 2007] serves as a possible explanation of the static fault endpoints documented here. Although our data do not bear directly on this interpretation, the orientation and current dimensions of the Ostler fault zone would thus reflect the length of an inherited, former Late Cretaceous – Miocene normal fault. Given the duration of active deformation on the Ostler fault since at least the Mid-Quaternary [*Davis et al.*, 2005], however, static endpoints on the Ostler fault zone may instead reflect barriers to propagation imposed by other nearby, long-lived structures. In either scenario, initial phases of fault growth would have likely been accompanied by rapid rates of tip propagation, followed by displacement accumulation at a nearly constant fault length [*Walsh et al.*, 2002].

7. Conclusion

[76] Deformed strath and outwash terraces along the entire Ostler fault zone provide rare, field-based kinematic constraints on the spatiotemporal growth of an active thrust fault. Integration of displacement measurements from multiple transverse drainages spanning the length of the Ostler fault, coupled with time control on several generations of terrace surfaces, enables resolution of transport-parallel and –perpendicular fault growth with unprecedented clarity. Taken together, these measurements reveal remarkably persistent spatial and temporal patterns of displacement accumulation throughout the Late Quaternary.

[77] Strike-perpendicular fold growth along the Ostler fault occurs mainly through progressive backlimb tilting and formation of highly asymmetric anticlines with steep, abrupt forelimbs and gentle backlimbs, suggesting deformation over a listric thrust. Other locations along the fault exhibit uniform differential uplift of terrace treads without significant tilting, consistent with transport above a planar fault ramp [*Hardy and Poblet*, 2005], although neither style of deformation is strictly associated with bedrock type. Predicted subsurface geometries suggest that curved fault planes transition downward into gently dipping, planar ramps at relatively shallow depths of less than ~1.5 km. The depth of this transition is greatest along the southern Ostler fault, where the degree of listric curvature also generally lower than northern fault sections. Abrupt changes in fault geometry generally correspond to major section boundaries.

[78] Fault displacement and slip-rate measurements from folded terraces and fault scarp profiles suggest that along-strike growth of the Ostler fault over the last ~70–105 k.y. reflects steady amplification of the displacement profile at a roughly constant fault length. These data imply that the fault endpoints were generally static and that displacement accumulated without significant lateral fault propagation. Displacement profiles along major fault sections exhibit varying degrees of asymmetry and broad, smoothly varying gradients in slip that are generally greatest near the fault tips in zones of fault overlap. Complementary asymmetry in overlapping displacement profiles suggests that slip transfer and interaction among fault segments occurs at scales ranging from individual scarps [*Davis et al.*, 2005] to major sections that constitute the entire fault zone. The temporal persistence of elevated displacement and slip-rate gradients in transfer zones or areas of segment overlap reflects this interaction and the presence of potential barriers to lateral propagation [*Nicol et al.*, 1996]. Over this time interval, maximum calculated slip rates for the Ostler fault zone reach values up to ~1.9 mm/yr, in general agreement with previously published estimates.

[79] Growth of the Ostler fault zone at a nearly constant length is consistent with the fault growth model of *Walsh et al.* [2002] and may reflect reactivation of a formerly extensional structure [*Ghisetti et al.*, 2007]. Given the apparent

pinning of the major fault tips, northward drainage diversion and wind-gap development on the Central Ostler section represent the product of sustained displacement gradients as slip accumulated during repeated coseismic events. The relatively pulsed nature of climatic variations controls formation of terrace surfaces and their subsequent incision. When this punctuated record is superimposed on steadier rates of tectonic displacement along the fault, it promotes the observed patterns of drainage deflection. These data contrast with more typical interpretations of progressive wind-gap emplacement as reflective of laterally propagating thrusts beneath growing anticlines [e.g., *Keller et al.*, 1998, 1999; *Jackson et al.*, 2002].

[80] Moreover, we develop additional field criteria to distinguish among models for fixed-length versus propagating faults, highlighting the importance of site-specific geomorphic and geochronologic data in unraveling lateral propagation histories from deformed wind gaps. Progressively abandoned wind gaps do not require significant propagation of the underlying fault, but can result from displacement above a fixed-length fault coupled with a geomorphic system that responds to pulsed climatic controls.

[81] **Acknowledgments.** We gratefully acknowledge the farmers and station owners in the Mackenzie Basin, specifically the Cameron, Campbell, Hocken, and Preston families, for making this work possible by granting access to their lands. Thanks to Julie Fosdick, Brian Clarke, and Adam Wade for help with fieldwork, and to Haikai Tane, David Nobes, and Jonathan Lapwood for discussion in the field. Dylan Rood provided assistance in modeling and interpreting CRN exposure ages. Helpful reviews by Bill Bull and Mike Taylor substantially improved the manuscript. We also thank NASA for providing the TOPSAR DEM of the study area. This research was supported by National Science Foundation grant EAR-0117242 and ACS Petroleum Research Fund grant 41960-AC8.

References

Abdrakhmatov, K. E., R. Weldon, S. Thompson, D. Burbank, C. Rubin, M. Miller, and P. Molnar (2001), Origin, direction, and rate of modern compression of the central Tien Shan (Kyrgyzstan), *Geol. Geofiz.*, *42*(10), 1585–1609.

Aitken, M. J. (1998), *An Introduction to Optical Dating: The Dating of Quaternary Sediments by the Use of Photon-Stimulated Luminescence*, 267 pp., Oxford Univ. Press, Oxford, U. K.

Amos, C. B., and D. W. Burbank (2007), Channel width response to differential uplift, *J. Geophys. Res.*, *112*, F02010, doi:10.1029/2006JF000672.

Amos, C. B., D. W. Burbank, D. C. Nobes, and S. A. L. Read (2007), Geomorphic constraints on listric thrust faulting: Implications for active deformation in the Mackenzie Basin, South Island, New Zealand, *J. Geophys. Res.*, *112*, B03S11, doi:10.1029/2006JB004291.

Balco, G., J. Stone, N. Lifton, and T. Dunai (2008), A simple, internally consistent, and easily accessible means of calculating surface exposure ages and erosion rates from Be-10 and Al-26 measurements, *Quat. Geochronol.*, *3*, 174–195, doi:10.1016/j.quageo.2007.12.001.

Bennett, E. R., J. H. Youngson, J. A. Jackson, R. J. Norris, G. M. Raisbeck, F. Yiou, and E. Fielding (2005), Growth of South Rough Ridge, Central Otago, New Zealand: Using in situ cosmogenic isotopes and geomorphology to study an active, blind reverse fault, *J. Geophys. Res.*, *110*, B02404, doi:10.1029/2004JB003184.

Bennett, E., J. Youngson, J. Jackson, R. Norris, G. Raisbeck, and F. Yiou (2006), Combining geomorphic observations with in situ cosmogenic isotope measurements to study anticline growth and fault propagation in Central Otago, New Zealand, *N. Z. J. Geol. Geophys.*, *49*(2), 217–231.

Bernal, A., S. Hardy, R. Gawthorpe, and E. Finch (2004), Stratigraphic expression of the lateral propagation and growth of isolated fault-related uplifts, *Basin Res.*, *16*(2), 219–233, doi:10.1111/j.1365-2117.2004.00230.x.

Blick, G. H., S. A. L. Read, and P. T. Hall (1989), Deformation monitoring of the Ostler fault zone, South Island, New Zealand, *Tectonophysics*, *167*, 329–339, doi:10.1016/0040-1951(89)90083-8.

Bookhagen, B., D. Fleitmann, K. Nishiizumi, M. R. Strecker, and R. C. Thiede (2006), Holocene monsoonal dynamics and fluvial terrace formation in the northwest Himalaya, India, *Geology*, *34*(7), 601–604, doi:10.1130/G22698.1.

Boyer, S. E., and D. Elliot (1982), Thrust systems, *AAPG Bull.*, *66*(9), 1196–1230.

Bull, W. B. (1991), *Geomorphic Responses to Climatic Change*, 326 pp., Oxford Univ. Press, New York.

Bull, W. B. (2007), *Tectonic Geomorphology of Mountains: A New Approach to Paleoseismology*, 320 pp., Blackwell, Oxford, U. K., doi:10.1002/9780470692318.

Bull, W. B. (2009), *Tectonically Active Landscapes*, 326 pp., Wiley-Blackwell, Oxford, U. K., doi:10.1002/9781444312003.

Bulnes, M., and K. McClay (1999), Benefits and limitations of different 2D algorithms used in cross-section restoration of inverted extensional faults: Application to physical experiments, *Tectonophysics*, *312*, 175–189, doi:10.1016/S0040-1951(99)00161-4.

Burbank, D. W., J. K. McLean, M. Bullen, K. Y. Abdrakhmatov, and M. M. Miller (1999), Partitioning of intermontane basins by thrust-related folding, Tien Shan, Kyrgyzstan, *Basin Res.*, *11*(1), 75–92, doi:10.1046/j.1365-2117.1999.00086.x.

Campbell, F. M., A. Kaiser, H. Horstmeyer, A. G. Green, F. Ghisetti, A. R. Gorman, M. Finnemore, and D. C. Nobes (2010), Processing and preliminary interpretation of noisy high-resolution seismic reflection/refraction data across the active Ostler fault zone, South Island, New Zealand, *J. Appl. Geophys.*, *70*, 332–342.

Cartwright, J. A., B. D. Trudgill, and C. S. Mansfield (1995), Fault growth by segment linkage: An explanation for scatter in maximum displacement and trace length data from the Canyonlands Grabens of SE Utah, *J. Struct. Geol.*, *17*(9), 1319–1326, doi:10.1016/0191-8141(95)00033-A.

Chamberlain, C. P., M. A. Poage, D. Craw, and R. C. Reynolds (1999), Topographic development of the Southern Alps recorded by the isotopic composition of authigenic clay minerals, South Island, New Zealand, *Chem. Geol.*, *155*, 279–294, doi:10.1016/S0009-2541(98)00165-X.

Chen, J., D. W. Burbank, K. M. Scharer, E. Sobel, J. H. Yin, C. Rubin, and R. B. Zhao (2002), Magnetochronology of the upper Cenozoic strata in the southwestern Chinese Tian Shan: Rates of Pleistocene folding and thrusting, *Earth Planet. Sci. Lett.*, *195*, 113–130, doi:10.1016/S0012-821X(01)00579-9.

Chen, J., R. Heermance, D. W. Burbank, K. M. Scharer, J. J. Miao, and C. S. Wang (2007), Quantification of growth and lateral propagation of the Kashi anticline, southwest Chinese Tian Shan, *J. Geophys. Res.*, *112*, B03S16, doi:10.1029/2006JB004345.

Childs, C., A. Nicol, J. J. Walsh, and J. Watterson (2003), The growth and propagation of synsedimentary faults, *J. Struct. Geol.*, *25*(4), 633–648, doi:10.1016/S0191-8141(02)00054-8.

Commins, D., S. Gupta, and J. Cartwright (2005), Deformed streams reveal growth and linkage of a normal fault array in the Canyonlands Graben, *Utah Geol.*, *33*(8), 645–648, doi:10.1130/G21433.1.

Cooper, K. A., S. Hardy, and R. Gawthorpe (2003), Stratigraphic and structural expression of the lateral growth of thrust fault-propagation folds: Results and implications from kinematic modelling, *Basin Res.*, *15*(2), 165–182, doi:10.1046/j.1365-2117.2003.00203.x.

Cowie, P. A., and G. P. Roberts (2001), Constraining slip rates and spacings for active normal faults, *J. Struct. Geol.*, *23*(12), 1901–1915, doi:10.1016/S0191-8141(01)00036-0.

Cowie, P. A., and C. H. Scholz (1992), Displacement length scaling relationship for faults: Data synthesis and discussion, *J. Struct. Geol.*, *14*(10), 1149–1156, doi:10.1016/0191-8141(92)90066-6.

Cowie, P. A., and Z. K. Shipton (1998), Fault tip displacement gradients and process zone dimensions, *J. Struct. Geol.*, *20*(8), 983–997, doi:10.1016/S0191-8141(98)00029-7.

Davis, K., D. W. Burbank, D. Fisher, S. Wallace, and D. Nobes (2005), Thrust-fault growth and segment linkage in the active Ostler fault zone, New Zealand, *J. Struct. Geol.*, *27*(8), 1528–1546, doi:10.1016/j.jsg.2005.04.011.

Dawers, N. H., and M. H. Anders (1995), Displacement-length scaling and fault linkage, *J. Struct. Geol.*, *17*(5), 607.

Dawers, N. H., M. H. Anders, and C. H. Scholz (1993), Growth of normal faults: Displacement-length scaling, *Geology*, *21*(12), 1107–1110, doi:10.1130/0091-7613(1993)021<1107:GONFDL>2.3.CO;2.

Deckart, H., U. Ring, and N. Mortimer (2002), Tectonic significance of Cretaceous bivergent extensional shear zones in the Torlesse accretionary wedge, central Otago Schist, New Zealand, *N. Z. J. Geol. Geophys.*, *45*(4), 537–547.

Delcaillau, B., B. Deffontaines, L. Floissac, J. Angelier, J. Deramond, P. Souquet, H. T. Chu, and J. F. Lee (1998), Morphotectonic evidence from lateral propagation of an active frontal fold: Pakuashan anticline, foothills of Taiwan, *Geomorphology*, *24*(4), 263–290, doi:10.1016/S0169-555X(98)00020-8.

DeMets, C., R. G. Gordon, D. F. Argus, and S. Stein (1994), Effect of recent revisions to the geomagnetic reversal time-scale on estimates of current plate motions, *Geophys. Res. Lett.*, *21*(20), 2191–2194, doi:10.1029/94GL02118.

Dolan, J. F., and J. P. Avouac (2007), Introduction to special section: Active fault-related folding: Structural evolution, geomorphologic expression, paleoseismology, and seismic hazards, *J. Geophys. Res.*, *112*, B03S01, doi:10.1029/2007JB004952.

Duller, G. A. T. (1996), Recent developments in luminescence dating of Quaternary sediments, *Prog.*

Phys. Geogr., *20*(2), 127–145, doi:10.1177/030913339602000201.

Elliott, D. (1976), Energy-balance and deformation mechanisms of thrust sheets, *Philos. Trans. R. Soc. London, A*, *283*(1312), 289–312.

Erslev, E. A. (1986), Basement balancing of Rocky-Mountain foreland uplifts, *Geology*, *14*(3), 259–262, doi:10.1130/0091-7613(1986)14<259:BBORMF>2.0.CO;2.

Erslev, E. A. (1991), Trishear fault-propagation folding, *Geology*, *19*(6), 617–620, doi:10.1130/0091-7613(1991)019<0617:TFPF>2.3.CO;2.

Eusden, J. D., J. R. Pettinga, and J. K. Campbell (2003), Structural collapse of a transpressive haningwall fault wedge, Charwell section of the Hope fault, South Island New Zealand, *Geol. Soc. Am. Abstr. Programs*, *35*, 63.

Formento-Trigilio, M. L., D. W. Burbank, A. Nicol, J. Shulmeister, and U. Rieser (2003), River response to an active fold-and-thrust belt in a convergent margin setting, North Island, New Zealand, *Geomorphology*, *49*(1–2), 125–152, doi:10.1016/S0169-555X(02)00167-8.

Gair, H. S. (1967), Sheet 20 - Mt. Cook. Geological Map of New Zealand, Dep. of Sci. and Indust. Res., Wellington, NZ.

Ghisetti, F. C., and R. H. Sibson (2006), Accommodation of compressional inversion in north-western South Island (New Zealand): Old faults versus new?, *J. Struct. Geol.*, *28*(11), 1994–2010, doi:10.1016/j.jsg.2006.06.010.

Ghisetti, F. C., A. R. Gorman, and R. H. Sibson (2007), Surface breakthrough of a basement fault by repeated seismic slip episodes: The Ostler fault, South Island, New Zealand, *Tectonics*, *26*, TC6004, doi:10.1029/2007TC002146.

Gold, R. D., E. Cowgill, X. F. Wang, and X. H. Chen (2006), Application of trishear fault-propagation folding to active reverse faults: Examples from the Dalong fault, Gansu Province, NW China, *J. Struct. Geol.*, *28*(2), 200–219, doi:10.1016/j.jsg.2005.10.006.

Gupta, A., and C. H. Scholz (2000), A model of normal fault interaction based on observations and theory, *J. Struct. Geol.*, *22*(7), 865–879, doi:10.1016/S0191-8141(00)00011-0.

Hancock, G. S., and R. S. Anderson (2002), Numerical modeling of fluvial strath-terrace formation in response to oscillating climate, *Geol. Soc. Am. Bull.*, *114*(9), 1131–1142.

Hardy, S., and C. D. Connors (2006), Short note: A velocity description of shear fault-bend folding, *J. Struct. Geol.*, *28*(3), 536–543, doi:10.1016/j.jsg.2005.12.015.

Hardy, S., and J. Poblet (1994), Geometric and numerical model of progressive limb rotation in detachment folds, *Geology*, *22*(4), 371–374, doi:10.1130/0091-7613(1994)022<0371:GANMOP>2.3.CO;2.

Hardy, S., and J. Poblet (2005), A method for relating fault geometry, slip rate and uplift data above fault-propagation folds, *Basin Res.*, *17*(3), 417–424, doi:10.1111/j.1365-2117.2005.00268.x.

Hetzel, R., M. Tao, S. Niedermann, M. R. Strecker, S. Ivy-Ochs, P. W. Kubik, and B. Gao (2004), Implications of the fault scaling law for the growth of topography: Mountain ranges in the broken foreland of north–east Tibet, *Terra Nova*, *16*(3), 157–162, doi:10.1111/j.1365-3121.2004.00549.x.

Hubert-Ferrari, A., J. Suppe, R. Gonzalez-Mieres, and X. Wang (2007), Mechanisms of active folding of the landscape (southern Tian Shan, China), *J. Geophys. Res.*, *112*, B03S09, doi:10.1029/2006JB004362.

Jackson, J., R. Norris, J. Youngson, and S. F. Wojtal (1996), The structural evolution of active fault and fold systems in central Otago, New Zealand: Evidence revealed by drainage patterns, *J. Struct. Geol.*, *18*(2–3), 217–234, doi:10.1016/S0191-8141(96)80046-0.

Jackson, J., J.-F. Ritz, L. Siame, G. Raisbeck, F. Yiou, R. Norris, J. Youngson, and E. Bennett (2002), Fault growth and landscape development rates in Otago, New Zealand, using in situ cosmogenic 10Be, *Earth Planet. Sci. Lett.*, *195*, 185–193, doi:10.1016/S0012-821X(01)00583-0.

Keller, E. A., R. L. Zepeda, T. K. Rockwell, T. L. Ku, and W. S. Dinklage (1998), Active tectonics at Wheeler Ridge, southern San Joaquin Valley, California, *Geol. Soc. Am. Bull.*, *110*(3), 298–310, doi:10.1130/0016-7606(1998)110<0298:ATAWRS>2.3.CO;2.

Keller, E. A., L. Gurrola, and T. E. Tierney (1999), Geomorphic criteria to determine direction of lateral propagation of reverse faulting and folding, *Geology*, *27*(6), 515–518, doi:10.1130/0091-7613(1999)027<0515:GCTDDO>2.3.CO;2.

Kim, Y. S., and D. J. Sanderson (2005), The relationship between displacement and length of faults: A review, *Earth Sci. Rev.*, *68*(3–4), 317–334, doi:10.1016/j.earscirev.2004.06.003.

Lal, D. (1991), Cosmic ray labeling of erosion surfaces: In situ nuclide production rates and erosion models, *Earth Planet. Sci. Lett.*, *104*, 424–439, doi:10.1016/0012-821X(91)90220-C.

Lavé, J., and J. P. Avouac (2000), Active folding of fluvial terraces across the Siwaliks Hills, Himalayas of central Nepal, *J. Geophys. Res.*, *105*, 5735–5770, doi:10.1029/1999JB900292.

Lisiecki, L. E., and M. E. Raymo (2005), A Pliocene-Pleistocene stack of 57 globally distributed benthic delta O-18 records, *Paleoceanography*, *20*, PA1003, doi:10.1029/2004PA001071.

Litchfield, N. J. (2001), The Titri fault system: Quaternary-active faults near the leading edge of the Otago reverse fault province, *N. Z. J. Geol. Geophys.*, *44*(4), 517–534.

Litchfield, N. J., and K. R. Berryman (2005), Correlation of fluvial terraces within the Hikurangi Margin, New Zealand: Implications for climate and baselevel controls, *Geomorphology*, *68*(3–4), 291–313, doi:10.1016/j.geomorph.2004.12.001.

Long, D. T., S. C. Cox, S. Bannister, M. C. Gerstenberger, and D. Okaya (2003), Upper crustal structure beneath the eastern Southern Alps and the Mackenzie Basin, New Zealand, derived from seismic reflection data, *New Zeal. J. Geol. Geophys.*, *46*(1), 21–39.

MacKinnon, T. C. (1983), Origin of the Torlesse terrane and coeval rocks, South Island, New Zealand, *Geol. Soc. Am. Bull.*, *94*(8), 967–985, doi:10.1130/0016-7606(1983)94<967:OOTTTA>2.0.CO;2.

Maizels, J. K. (1989), Differentiation of late Pleistocene terrace outwash deposits using geomorphic criteria: Tekapo Valley, South Island, New-Zealand, *N. Z. J. Geol. Geophys.*, *32*(2), 225–241.

Manighetti, I., G. C. P. King, Y. Gaudemer, C. H. Scholz, and C. Doubre (2001), Slip accumulation and lateral propagation of active normal faults in Afar, *J. Geophys. Res.*, *106*, 13,667–13,696, doi:10.1029/2000JB900471.

Martinson, D. G., N. G. Pisias, J. D. Hays, J. Imbrie, T. C. Moore, and N. J. Shackleton (1987), Age dating and the orbital theory of the ice ages: Development of a high-resolution-0 to 300,000-year chronostratigraphy, *Quat. Res.*, *27*(1), 1–29, doi:10.1016/0033-5894(87)90046-9.

McClymont, A. F., A. G. Green, P. Villamor, H. Horstmeyer, C. Grass, and D. C. Nobes (2008), Characterization of the shallow structures of active fault zones using 3-D ground-penetrating radar data, *J. Geophys. Res.*, *113*, B10315, doi:10.1029/2007JB005402.

Meyer, V., A. Nicol, C. Childs, J. J. Walsh, and J. Watterson (2002), Progressive localisation of strain during the evolution of a normal fault population, *J. Struct. Geol.*, *24*(8), 1215–1231, doi:10.1016/S0191-8141(01)00104-3.

Mildenhall, D. C. (2001), Pollen analysis of Pliocene-Pleistocene Kowai Formation (Kurow Group), Mackenzie Basin, South Canterbury, New Zealand, *N. Z. J. Geol. Geophys.*, *44*(1), 97–104.

Molnar, P., et al. (1994), Quaternary climate change and the formation of river terraces across growing anticlines on the north flank of the Tien Shan, China, *J. Geol.*, *102*, 583–602, doi:10.1086/629700.

Morewood, N. C., and G. P. Roberts (1999), Lateral propagation of the surface trace of the South Alkyonides normal fault segment, central Greece: Its impact on models of fault growth and displacement-length relationships, *J. Struct. Geol.*, *21*(6), 635–652, doi:10.1016/S0191-8141(99)00049-8.

Mueller, K., and P. Talling (1997), Geomorphic evidence for tear faults accommodating lateral propagation of an active fault-bend fold, Wheeler Ridge, California, *J. Struct. Geol.*, *19*(3–4), 397–411, doi:10.1016/S0191-8141(96)00089-2.

Muraoka, H., and H. Kamata (1983), Displacement distribution along minor fault traces, *J. Struct. Geol.*, *5*(5), 483–495, doi:10.1016/0191-8141(83)90054-8.

Nicol, A., and J. K. Campbell (2001), The impact of episodic fault-related folding on late Holocene degradation terraces along Waipara River, New Zealand, *N. Z. J. Geol. Geophys.*, *44*(1), 145–156.

Nicol, A., J. Watterson, J. J. Walsh, and C. Childs (1996), The shapes, major axis orientations and displacement patterns of fault surfaces, *J. Struct. Geol.*, *18*(2–3), 235–248, doi:10.1016/S0191-8141(96)80047-2.

Nicol, A., J. Walsh, K. Berryman, and S. Nodder (2005), Growth of a normal fault by the accumulation of slip over millions of years, *J. Struct. Geol.*, *27*(2), 327–342, doi:10.1016/j.jsg.2004.09.002.

Norris, R. J., and A. F. Cooper (2001), Late Quaternary slip rates and slip partitioning on the Alpine fault, New Zealand, *J. Struct. Geol.*, *23*(2–3), 507–520, doi:10.1016/S0191-8141(00)00122-X.

Pan, B., D. Burbank, Y. Wang, G. Wu, J. Li, and Q. Guan (2003), A 900 k.y. record of strath terrace formation during glacial-interglacial transitions in northwest China, *Geology*, *31*(11), 957–960, doi:10.1130/G19685.1.

Pazzaglia, F. J., and M. T. Brandon (2001), A fluvial record of long-term steady-state uplift and erosion across the Cascadia forearc high, western Washington State, *Am. J. Sci.*, *301*(4–5), 385–431, doi:10.2475/ajs.301.4-5.385.

Peacock, D. C. P., and D. J. Sanderson (1991), Displacements, segment linkage and relay ramps in normal-fault zones, *J. Struct. Geol.*, *13*(6), 721–733.

Peacock, D. C. P., and D. J. Sanderson (1996), Effects of propagation rate on displacement variations along faults, *J. Struct. Geol.*, *18*(2–3), 311–320.

Pearson, C. F., J. Beavan, D. J. Darby, G. H. Blick, and R. I. Walcott (1995), Strain distribution across the Australian-Pacific plate boundary in the central South Island, New Zealand, from 1992 GPS and earlier terrestrial observations, *J. Geophys. Res.*, *100*, 22,071–22,081, doi:10.1029/95JB02279.

Petit, J. R., et al. (1999), Climate and atmospheric history of the past 420,000 years from the Vostok ice core, Antarctica, *Nature*, *399*, 429–436, doi:10.1038/20859.

Pinter, N., B. Johns, B. Little, and W. Dean Vestal (2001), Fault-related folding in California's northern Channel Islands documented by rapid-static GPS positioning, *GSA Today*, *11*(5), 4–9, doi:10.1130/1052-5173(2001)011<0004:FRFICN>2.0.CO;2.

Poblet, J., and K. McClay (1996), Geometry and kinematics of single-layer detachment folds, *AAPG Bull.*, *80*(7), 1085–1109.

Poulimenos, G. (2000), Scaling properties of normal fault populations in the western Corinth Graben, Greece: Implications for fault growth in large strain settings, *J. Struct. Geol.*, *22*(3), 307–322, doi:10.1016/S0191-8141(99)00152-2.

Pratt, B., D. W. Burbank, A. Heimsath, and T. Ojha (2002), Impulsive alluviation during early Holocene strengthened monsoons, central Nepal Himalaya, *Geology*, *30*(10), 911–914, doi:10.1130/0091-7613(2002)030<0911:IADEHS>2.0.CO;2.

Prescott, J. R., and J. T. Hutton (1994), Cosmic-ray contributions to dose-rates for luminescence and Esr dating: Large depths and long-term time variations, *Radiat. Meas.*, *23*(2–3), 497–500.

Preusser, F., B. G. Andersen, G. H. Denton, and C. Schluchter (2005), Luminescence chronology of late Pleistocene glacial deposits in North Westland, New Zealand, *Quat. Sci. Rev.*, *24*, 2207–2227, doi:10.1016/j.quascirev.2004.12.005.

Read, S. A. L. (1984), The Ostler fault zone, in *Guidebook to the South Island Scientific Excursions International Symposium on Recent Crustal Movements of the Pacific Region*, edited by P. R. Wood, pp. 121–134, R. Soc. of N. Z., Wellington.

Read, S. A. L., and G. H. Blick (1991), Late Quaternary deformation and geodetic monitoring in the area of "the knot" on the Ostler fault zone, South Island, New Zealand, *N. Z. Geol. Surv. Rec.*, *43*, 85–91.

Rockwell, T. K., E. A. Keller, M. N. Clark, and D. L. Johnson (1984), Chronology and rates of faulting of Ventura River terraces, California, *Geol. Soc. Am. Bull.*, *95*(12), 1466–1474, doi:10.1130/0016-7606(1984)95<1466:CAROFO>2.0.CO;2.

Schaefer, J. M., U. Ninnemann, G. H. Denton, C. Schluechter, S. Ivy-Ochs, R. Wieler, P. W. Kubik, B. G. Anderson, and P. Schlosser (2001), Structure of the last glacial maximum in New Zealand: Terrestrial and marine evidence from southern mid-latitudes, *Eos. Trans. AGU*, *82*(47), Fall Meet. Suppl., Abstract PP42B–0499.

Schaefer, J. M., G. H. Denton, D. J. A. Barrell, S. Ivy-Ochs, P. W. Kubik, B. G. Andersen, F. M. Phillips, T. V. Lowell, and C. Schluchter (2006), Near-synchronous interhemispheric termination of the last glacial maximum in mid-latitudes, *Science*, *312*(5779), 1510–1513, doi:10.1126/science.1122872.

Scharer, K. M., D. W. Burbank, J. Chen, and R. J. I. Weldon (2006), Kinematic models of fluvial terraces over active detachment folds: Constraints on the growth mechanism of the Kashi-Atushi fold system, Chinese Tian Shan, *Geol. Soc. Am. Bull.*, *118*(7), 1006–1021, doi:10.1130/B25835.1.

Schlische, R. W., S. S. Young, R. V. Ackermann, and A. Gupta (1996), Geometry and scaling relations of a population of very small rift-related normal faults, *Geology*, *24*(8), 683–686, doi:10.1130/0091-7613(1996)024<0683:GASROA>2.3.CO;2.

Schwartz, D. P., and K. J. Coppersmith (1984), Fault behavior and characteristic earthquakes: Examples from the Wasatch and San-Andreas fault zones, *J. Geophys. Res.*, *89*, 5681–5698, doi:10.1029/JB089iB07p05681.

Seeber, L., and C. C. Sorlien (2000), Listric thrusts in the western Transverse Ranges, California, *Geol. Soc. Am. Bull.*, *112*(7), 1067–1079, doi:10.1130/0016-7606(2000)112<1067:LTITWT>2.0.CO;2.

Simoes, M., J. P. Avouac, Y. G. Chen, A. K. Singhvi, C. Y. Wang, M. Jaiswal, Y. C. Chan, and S. Bernard (2007), Kinematic analysis of the Pakuashan fault tip fold, west central Taiwan: Shortening rate and age of folding inception, *J. Geophys. Res.*, *112*, B03S14, doi:10.1029/2005JB004198.

Sporli, K. B., and A. R. Lillie (1974), Geology of the Torlesse supergroup in the northern Ben-Ohau Range, Canterbury, *N. Z. J. Geol. Geophys.*, *17*(1), 115–141.

Stein, R. S., and G. C. P. King (1984), Seismic potential revealed by surface folding - 1983 Coalinga, California, *Earth Sci.*, *224*(4651), 869–872.

Stone, J. O. (2000), Air pressure and cosmogenic isotope production, *J. Geophys. Res.*, *105*, 23,753–23,759, doi:10.1029/2000JB900181.

Suggate, R. P. (1990), Late Pliocene and Quaternary glaciations of New Zealand, *Quat. Sci. Rev.*, *9*, 175–197, doi:10.1016/0277-3791(90)90017-5.

Suppe, J. (1983), Geometry and kinematics of fault-bend folding, *Am. J. Sci.*, *283*(7), 684–721.

Suppe, J., and D. A. Medwedeff (1990), Geometry and kinematics of fault-propagation folding, *Eclogae Geol. Helv.*, *83*(3), 409–454.

Suppe, J., G. T. Chou, and S. C. Hook (1992), Rates of folding and faulting determined from growth strata, in *Thrust Tectonics*, edited by K. R. McClay, pp. 105–121, Chapman and Hall, London.

Suppe, J., C. D. Connors, and Y. Zhang (2004), Shear fault-bend folding, *AAPG Mem.*, edited by K. R. McClay, *82*, 303–323.

Sutherland, R., K. Kim, A. Zondervan, and M. McSaveney (2007), Orbital forcing of mid-latitude Southern Hemisphere glaciation since 100 ka inferred from cosmogenic nuclide ages of moraine boulders from the Cascade Plateau, southwest New Zealand, *Geol. Soc. Am. Bull.*, *119*(3), 443–451.

Templeton, A. S., D. Craw, P. O. Koons, and C. P. Chamberlain (1999), Near-surface expression of a young mesothermal gold mineralizing system, Sealy range, Southern Alps, New Zealand, *Miner. Deposita*, *34*(2), 163–172, doi:10.1007/s001260050193.

Thompson, S. C., R. J. Weldon, C. M. Rubin, K. Abdrakhmatov, P. Molnar, and G. W. Berger (2002), Late Quaternary slip rates across the central Tien Shan, Kyrgyzstan, central Asia, *J. Geophys. Res.*, *107*(B9), 2203, doi:10.1029/2001JB000596.

Tippett, J. M., and N. Hovius (2000), Geodynamic processes in the Southern Alps, New Zealand, in *Geomorphology and Global Tectonics*, edited by M. A. Summerfield, pp. 109–134, John Wiley, Chichester, U. K.

Upton, P., P. O. Koons, D. Craw, C. M. Henderson, and R. Enlow (2009), Along-strike differences in the Southern Alps of New Zealand: Consequences of inherited variation in rheology, *Tectonics*, *28*, TC2007, doi:10.1029/2008TC002353.

van Dissen, R. J., A. G. Hull, and S. A. L. Read (1994), Timing of some large Holocene earthquakes on the Ostler fault, New Zealand, paper presented at Eighth International Symposium on Recent Crustal Movements, pp. 381–386, Geod. Soc. of Jpn., Kobe.

Villamor, P., R. Van Dissen, B. V. Alloway, A. S. Palmer, and N. Litchfield (2007), The Rangipo fault, Taupo rift, New Zealand: An example of temporal slip-rate and single-event displacement variability in a volcanic environment, *Geol. Soc. Am. Bull.*, *119*(5), 529–547, doi:10.1130/B26000.1.

Wallace, S. C., D. C. Nobes, K. J. Davis, D. W. Burbank, and A. White (2010), Three-dimensional GPR imaging of the Benmore anticline and step-over of the Ostler fault, South Island, New Zealand, *Geophys. J. Int.*, *180*(2), 465–474, doi:10.1111/j.1365-246X.2009.04400.x.

Walsh, J. J., and J. Watterson (1988), Analysis of the relationship between displacements and dimensions of faults, *J. Struct. Geol.*, *10*(3), 239–247, doi:10.1016/0191-8141(88)90057-0.

Walsh, J. J., A. Nicol, and C. Childs (2002), An alternative model for the growth of faults, *J. Struct. Geol.*, *24*(11), 1669–1675, doi:10.1016/S0191-8141(01)00165-1.

Ward, C. M., and K. B. Sporli (1979), Exceptionally large steeply plunging folds in the Torlesse Terrace, New Zealand, *J. Geol.*, *87*, 187–193.

C. B. Amos, Department of Earth and Planetary Science, University of California, Berkeley, CA 94720, USA. (cbamos@seismo.berkeley.edu)

D. W. Burbank, Institute for Crustal Studies, University of California, Santa Barbara, CA 93106, USA. (burbank@crustal.ucsb.edu)

S. A. L. Read, Institute of Geological and Nuclear Sciences Ltd., PO Box 30-368, Lower Hutt, 6009, New Zealand. (S.Read@gns.cri.nz)